A seismic tomography, gravity, and flexure study of the crust and upper mantle structure of the Hawaiian Ridge, Part 1

B. G. MacGregor[1], R. A. Dunn[1,*], A. B. Watts[2], C. Xu[2,3], and D. J. Shillington[4]

[1]Department of Earth Sciences, School of Ocean and Earth Science and Technology, University of Hawai‘i at Manoa, Honolulu, HI, USA.
[2]Department of Earth Sciences, University of Oxford, Oxford, UK.
[3]Key Lab of Submarine Geosciences and Prospecting Techniques, Ministry of Education, and College of Marine Geosciences, Ocean University of China, Qingdao, China.
[4]School of Earth and Sustainability, Northern Arizona University, Flagstaff, AZ, USA.

*Corresponding author: R. A. Dunn (dunnr@hawaii.edu)

Abstract

The Hawaiian Ridge has long been a focus site for studying lithospheric flexure due to intraplate volcano loading, but crucial load and flexure details remain unclear. We address this problem using wide-angle seismic refraction and reflection data acquired along a ~535-km-long profile that intersects the ridge between the islands of Maui and Hawai‘i and crosses 80-95 Myr-old lithosphere. A tomographic image constructed using travel time data of several seismic phases reveals broad flexure of Pacific oceanic crust extending up to ~200-250 km either side of the Hawaiian Ridge, and vertically up to ~6-7 km. The *P*-wave velocity structure, verified by gravity modelling, reveals that the west flank of Hawaii is comprised of extrusive lavas overlain by volcanoclastic sediments and a carbonate platform. In contrast, the Hāna Ridge, southeast of Maui, contains a high-velocity core consistent with mafic or ultramafic intrusive rocks. Magmatic underplating along the seismic line is not evident. Reflectors at the top and bottom of the pre-existing oceanic crust suggest a ~4.5-6 km crustal thickness. Simple three-dimensional flexure modelling with an elastic plate thickness, T_e, of 26.7 km shows that the depths to the reflectors beneath the western flank of Hawai’i can be explained by volcano loading in which Maui and the older islands in the ridge contribute ~43% to the flexure and the island of Hawai‘i ~51%. Previous studies, however, revealed a higher T_e beneath the eastern flank of Hawai’i suggesting that isostatic compensation may not yet be complete at the youngest end of the ridge.

Plain Language Summary

The Hawaiian Islands are one of Earth's best examples of a volcanic chain that formed on a tectonic plate that is moving over a fixed hotspot in the deep mantle. They are a 'natural laboratory' for the study of intraplate volcanism and their impact on the large-scale deformation of the plates. We carried out a seismic imaging experiment along a ~535-km-long profile that intersected the chain between the islands of Maui and Hawai‘i. The seismic velocity image reveals a high velocity, high density, 'core' to part of the chain and that the combined weight of the edifices that make up each island has flexed the Pacific oceanic plate down by up to ~6-7 km over distances of up to 400-500 km. There is evidence that the elastic thickness of the Pacific lithosphere may be higher for Hawai‘i than for the older islands in the Hawaiian ridge, suggesting that the adjustment to volcanic loading is still on-going at the youngest end of the chain.

1. Introduction

The Hawaiian Ridge is an intraplate volcanic chain of seamounts and subaerial islands in the central and northwest Pacific Ocean, long believed to have been created by pressure-release melting within a rising mantle plume (e.g., Morgan, 1971; Wilson, 1963). As each successive volcano in the Hawaiian Ridge is emplaced, its large mass deforms the Earth's surface, resulting in a deflection or flexure of the lithosphere (e.g., Gunn, 1943; Suyenaga, 1979; Walcott, 1970; Watts, 2023; Watts & Cochran, 1974; Watts & ten Brink, 1989; Wessel, 1993a). The eastern extent of the ridge, largely composed of the Hawaiian Islands, is an example of a young surface load emplaced on relatively old (~90 Ma) lithosphere (Seton et al., 2020) that may still be undergoing some form of load-induced viscoelastic relaxation (e.g., Watts & Zhong, 2000; Zhong & Watts, 2013).

The flexure is readily apparent in regional bathymetry and gravity anomaly data (Figure 1). Bathymetry data reveal a depression flanking the ridge known as the Hawaiian Moat. The moats are typically ~0.7 km deeper than the adjacent ocean floor (Hamilton, 1957), and are partially filled with volcanoclastic material, pelagic sediments, and the products of mass wasting from the ridge (Leslie et al., 2002; Rees et al., 1993; ten Brink & Watts, 1985; Tribble et al., 1993; Wolfe et al., 1994). The ridge and flanking moats are superimposed on a long-wavelength bathymetric swell up to ~1000 km in width and ~1.5 km in height above the regional seafloor depth (Dietz & Menard, 1953). Superimposed on the swell is the Hawaiian Arch, lying ~250-300 km from the axis of the ridge (Klein, 2016; Watts, 2023; Watts &

Cochran, 1974; Watts & ten Brink, 1989; Wessel, 1993b). Free-air gravity anomaly data (e.g., Watts & Talwani, 1975) reveal positive anomalies of up to +700 mGal over the ridge that are flanked by negative anomalies of up to -125 mGal over the moats. This negative-positive-negative pattern of anomalies is superimposed on a long wavelength positive anomaly of up to +35 mGal that is associated with the mass excess of the swell and the mass deficiency of its compensation. The long wavelength gravity/bathymetry ratio is therefore ~23 mGal/km and the swell has been attributed to some form of convection in the mantle (e.g., Watts, 1976) that is generated by buoyancy forces of thermal (e.g., Leahy et al., 2010) and compositional (e.g., Rychert et al., 2013) origin.

The most direct evidence of flexure along the Hawaiian Ridge has come from seismic reflection and refraction profile data. Shor & Pollard (1964) found, using shots at sea and towed hydrophones north of Maui, that the depth of Moho below sea level increases from 10.5 km beneath the arch to 13 km beneath the moat and ridge. On the shallow shelf east of Maui and south of O‘ahu, Furumoto & Woollard (1965) found depths to Moho of 15.4 km and 21.5 km, respectively. Zucca et al. (1982), using shots at sea and stations on Hawai‘i, found that Moho dips toward the center of the edifice increasing from ~10 km offshore at the edge of the edifice to ~17-19 km beneath the summit of the edifice, a depth offset of ~7-9 km.

The first experiment to use a multichannel seismic technique to specifically address flexure along the Hawaiian Ridge was carried out in 1982 onboard the R/V *Robert D. Conrad* and R/V *Kana Keoki* (Watts et al., 1985). Three 500-km-long seismic reflection and refraction profiles were acquired (Figure 1a), which intersected the Hawaiian Ridge between O‘ahu and Moloka‘i, and O‘ahu and Kaua‘i. The experiment, which included two-ship Constant Offset Profiles (COPs) to profile prominent reflectors and Expanding Spread Profiles (ESPs) to determine the *P* wave velocity structure, showed the depth to Moho increased from ~11 km beneath the arch to >14 km beneath the ridge. It also indicated that loads in the hotspot-generated Hawaiian Ridge progressively flexed the pre-existing oceanic crust (e.g., Watts & ten Brink, 1989; Wolfe et al. 1994) such that new volcanoes influenced the subsidence and uplift history of pre-existing volcanoes and that the flexed oceanic crust may be underplated by magmatic material (ten Brink & Brocher, 1987).

In 1998, Park et al. (2007) conducted a seismic study of the south-east flank of Hawai‘i in which they employed a combination of refraction tomography, including a wide grid pattern of shots from the R/V *Ewing* and land-based seismographs, and multichannel seismic reflection profiling. They showed that Moho increases in depth from ~12 km at a position 45 km seaward of the coast to >15 km beneath Mauna Loa, a depth change of >3 km. Within the crust, Park et al. (2007) identified several zones of high *P*-wave velocity (>7 km/s), which they interpreted as deep magma reservoirs to the volcanic centers of Kīlauea's eastern rift zone and Mauna Loa's southwest rift zone.

Despite these and other earlier experiments, we still know little of the internal seismic structure of the Hawaiian Ridge and the details of the response of the lithosphere to volcano loading. This is particularly the case for the youngest island along the ridge – Hawaiʻi. Knowing the details of the internal *P* wave velocity structure of a volcanic edifice and its flanking moats is important when calculating load and infill densities, the proportion of surface to sub-surface volcanic loads and the effective elastic thickness, a proxy for the long-term strength of oceanic lithosphere. As several studies have shown, the elastic thickness and its relationship to the age of the oceanic lithosphere at the time of loading have provided important constraints not only on the tectonic setting of bathymetric features on the seafloor (e.g., Watts et al., 1990; 2006) but on the rheology of oceanic lithosphere at lithospheric conditions (e.g., Zhong & Watts, 2013).

In 2018, we conducted the first marine wide-angle seismic tomography and gravity experiment across the Hawaiian Ridge, as part of a broader study of the seismic structure of the Hawaiian-Emperor Seamount Chain (Boston et al., 2019; Watts et al., 2021; Xu et al., 2022). In this paper, we report results from a single seismic and gravity profile (Line 01) located along the north-west flank of Hawaiʻi and the eastern flank of Maui. In a companion paper by Dunn et al. (2023), we report in data from a seismic and gravity profile (Line 02) located along the north-west flank of the Island of O'ahu. The two papers investigate volcano structures and plate loading and flexure for two very different load sizes. Here, our findings reveal that the Hawaiian Ridge consists of volcanic edifices over 9 km thick, which overlay pre-existing Pacific oceanic crust with a thickness of ~4.5-6 km. The volcanic load produces a broad flexural response of the Pacific lithosphere with a peak vertical downward deflection of 6-7 km. The results obtained from seismic tomography, validated through gravity modelling, are utilized to estimate the elastic thickness of the Pacific oceanic lithosphere.

2. Experiment and Geological Setting

During September - October 2018, seismic refraction and reflection and gravity anomaly data were collected along a ~535-km-long line located just west of the island of Hawaiʻi

(Figures 1 and 2). Thirty-five ocean bottom seismographs (OBS) were deployed along the line and the seismic source was the 36-gun 6600-cubic-inch airgun array of the R/V *Marcus G. Langseth*, towed at a water depth of 12 m. Each OBS contained a 3-component geophone and a hydrophone that recorded with a sampling rate of 200 samples/s. These sensors were spaced ~15 km apart and the line was shot twice, once at intervals of ~390 m for wide-angle data, which will be referred to as the OBS shots, and again at ~62.5 m intervals while towing a seismic streamer, which will be referred to as the MCS shots. The OBS recorded both sets of shots, and both sets of OBS-recorded data are included in this analysis. The MCS shots provide dense coverage at short ranges, and a more limited amount of long-range data that varied from station to station.

The seismic line intersects the Hawaiian Ridge west of the island of Hawaiʻi, crossing the flanks of the volcanoes of Māhukona and Kohala, and the large volcanic rift system of East Maui known as the Hāna Ridge (Figure 2). Māhukona has been studied in detail with submersible dives, dredging and geophysical methods (Garcia et al., 2012). Recovered lavas from Māhukona were $^{40}Ar/^{39}Ar$ dated, and estimated to have erupted as late-shield tholeiitic and post-shield transitional volcanism (~0.650 Ma - ~0.325 Ma). Māhukona is geochemically diverse, having lavas with both Mauna Kea and Mauna Loa source signatures (Garcia et al., 2012).

The line also crosses Cretaceous Seamounts located to the south of the Hawaiian Ridge, at least two large landslide deposits located on the flanks of the Hawaiian Ridge, and the Molokaʻi Fracture Zone (MFZ) (Figure 2). The Cretaceous Seamounts were probably formed on or near a mid-ocean ridge axis (Fornari & Campbell, 1987). The most prominent seamounts from this chain in our study area are Cook and Jaggar Seamounts (Figure 2), which rise up to ~5 km above the seafloor, with Jaggar being the larger of the two (Bridges, 1997). The Indianapolis Seamount is a smaller feature standing ~2 km above the regional seafloor depth, located just to the northeast of Cook and Jaggar. Many details of these seamounts (including their internal structure) are unknown. The seismic line crosses the Alika 2 landslide and Hāna Slump, located on the northwest flank of Hawaiʻi Island and on the north flank of Hāna Ridge, respectively (Figure 2). The Alika 2 Slide resulted from gravitational failure of the southwest flank of Mauna Loa (Lipman et al., 1988). It has been mapped using the GLORIA's side-scan sonar system. Integration of these data have led to an estimate of the thickness of this landslide deposit to be ~20-200 m and the volume to be ~200-600 km^3. The seismic line crosses hummocks and isolated blocks of slide material that broke off from Mauna Loa's upper submarine and subaerial flanks (Lipman et al., 1988). Two drill cores determined the Alika 2 Slide events to have occurred rapidly between 112 ± 15 ka and 127 ± 5 ka using ^{230}Th dating and oxygen isotope analysis respectively (McMurtry et al., 1999). The Hāna Slump covers an area of ~4,000 km^2, with transverse ridges and basins at its toe on the northeast of the slump (Eakins & Robinson, 2006) (Figure 2). The northwest portion of the slump is morphologically smooth and is estimated to contain a ~1-km-thick layer of volcaniclastic sediment. The southeast portion of the slump transitions over a 10-km wide zone from low sonar backscatter to a higher backscatter region where it intersects the Hāna Ridge. The low sonar backscatter is a strong indication of a smooth, sediment blanket on the southeast portion of the slump (Eakins & Robinson, 2006).

In the northeast, the seismic line crosses the MFZ, a broad, late-Cretaceous feature with two primary sets of strands located ~100 km apart (Figure 2), both arcing to the southwest (Figure 1b). Trend differences between individual strands can be attributed to a ~10°clockwise change of Pacific-Farallon spreading direction at the time of formation (Searle et al., 1993). Magnetic anomaly patterns surrounding the MFZ area are incomplete and difficult to interpret. Nevertheless, the age difference between the regions north and south of the MFZ appears to be ~12-16 Myr, with the south being older (Atwater & Menard, 1970; Seton et al., 2020). The Hawaiian Ridge grew across the top of the MFZ.

3. Seismic Data Processing and Interpretations

After recovery of the OBS, the data were clock-corrected and converted to SEG-Y files. Initially, the data were filtered with a minimum-phase 5–45 Hz Butterworth filter and the water wave and its first multiple were picked for shots that occurred within a few km of each instrument. By comparing the first arrival to its multiple (after correcting for a small difference in path length) a consistent shot time bias of ~150 ms was detected across all instruments. Xu et al. (2022) found a similar bias and suggested this is due to a difference between the firing cue given to the airgun array and the time at which the air bubble is released by the mechanical shuttles and forms a coherent pressure wave. The time shift of 150 ms was applied to the time base of each OBS. The location of each OBS on the seafloor was then calculated from the direct water wave travel times using a Bayesian grid-search algorithm (Dunn & Hernandez, 2009).

Prior to travel-time picking of solid-earth seismic phases, the seismic data were re-filtered with a 5-25 Hz Butterworth filter and a gain was applied to adjust for range-dependent energy loss. For display, a simple correction for seafloor topography was applied to facilitate phase identification (computed as the difference in travel time for 1-D seismic models with and without seafloor topography). Trace-to-trace averaging was applied to assist in identifying first arrivals in some record sections with noisy data (which worked well for the closely-spaced MCS records), and predictive deconvolution was applied in some cases to assist in identifying secondary arrivals. Due to different levels of time-dependent noise, the seismic phases were picked on both the hydrophone (*H*) and vertical geophone (*Z*) channels to capture the best quality data of either channel. MCS shots were mostly picked on channel *H*. A variety of seismic phases were identified, and as described below, the presence and timing of a particular phase is largely dependent on the geologic setting (e.g., old oceanic crust or the Hawaiian ridge). A total of ~61,300 travel times were obtained (Table 1). A set of records from each station can be found in the online Supporting Information (Figure S1) that accompanies this paper.

3.1 Stations located to the south of the Hawaiian Ridge

Stations located to the south of the Hawaiian Ridge show standard seismic phases for oceanic crust. These phases include *P*-wave refractions that, following common practice (e.g., Bratt & Purdy, 1984; Raitt, 1963), are interpreted to occur in the sediment layer (*P1*), the upper basaltic crust (*P2*), lower gabbroic crust (*P3*), and mantle (*Pn*) (Figure 3a south). Also observed are *P*-wave reflections from the top of the mantle (*PmP*), and a shallow triplication or reflection-like phase (*P2P*) that marks the transition between *P1* (<5 km/s) and *P2* (5-6.5 km/s) refractions. *P2P* is most obvious across the deeper moat areas, where the records indicate sediments are thickest, as compared to outside of the moat areas, where sediments appear to be thinner and the correct identification of *P2P* arrivals is more difficult. The interpretation of *P2P*, as the top of oceanic crust or a deeper transition, such as the layer 2A-2B transition, is discussed in the Results Section. The transition between the *P2* and *P3* refractions is often gradual, usually without an obvious triplication or sharp change in apparent velocity. We chose 6-6.5 km/s to mark the transition from *P2* to *P3*, and while this is arbitrary, it does not affect tomographic imaging since the two phases are treated as one in the imaging. There is no evidence in the records for a broad low-velocity upper-mantle layer that underplates the oceanic crust, as has been suggested by a prior seismic receiver function study (Leahy et al., 2010).

Beneath the Cook and Jaggar seamounts, we observe a different suite of phases (Figures 3a north and 3b). There is a refracted phase from the interior of the seamounts (*Pv*), and two reflection-like phases. One from near the top of the seamounts (*PvP*), at the base of a shallow low-Vp layer, and the other from beneath the seamounts (*P2P*), at what is presumably the top, or near the top, of the Cretaceous oceanic crust. Here, *PvP* marks the change in vertical velocity gradient between the *P1* and *Pv* refractions, while *P2P* is associated with the change between *Pv* and *P2*. In the region between the Hawaiian Ridge and the seamounts, the records indicate that the sediment layer is relatively thicker. *P1* extends to relatively large ranges and *P2P* is relatively delayed in time and range. Figure 3c shows examples of these phases for station 111, located in the moat between these geological features.

3.2 Stations located to the north of the Hawaiian Ridge

North of the Hawaiian Ridge, across the broadly-spaced strands of the MFZ, the seismic records indicate the local crustal structure deviates markedly from a standard Pacific oceanic crustal structure (Figure 4). While the low-velocity phase, *P1*, is generally present, the crustal phases *P2* and *P3* are in many cases limited in range or not obvious, and the range to where *Pn* is a first arrival is greatly reduced as compared to a 6-km-thick crust (<20 km versus the more typical ~30-35 km). The *PmP* phase is often more limited in the range over which it can be identified and has variable character, possibly due to some combination of a more variable crustal structure and a more variable Moho character or depth. Therefore, overall, the records indicate that the crust is thinner and more variable across this region, and this is probably related to the presence of the fracture zone.

3.3 Stations located across the Hawaiian Ridge

Across the crest of the volcanic edifices, a refraction within the edifice (*Pv*) dominates the earlier parts of record sections. Just beyond the range of *P1*, *Pv* is a first arrival with apparent velocities around 5 km/s (Figure 5). *Pv* is often observed to shot-receiver distances of up to 40-50 km. This large offset suggests the edifice material is several kilometers thick. At the junction between *P1* and *Pv*, is a triplication or reflection-like feature in the data that was assigned the phase name *PvP*, as was done for a similar phase beneath the seamounts. The range to the cross-over point is small but variable (~2-10 km). Across the edifice the *PmP* phase is regularly observed at ~40-60 km, or more, again indicating a thick edifice structure, and *Pn* extends beyond with an average apparent velocity of about 8 km/s, though edifice structure greatly affects the local slope of the travel time curves. There is no clear evidence for a low-velocity (~7.4-7.8 km/s) upper-mantle layer that underplates the ridge in this area, as was suggested by earlier active-source studies to the east of the island of O‘ahu (e.g., ten Brink & Brocher, 1987; Watts et al, 1985).

Behind the long *Pv* branch is a set of arrivals consistent with the presence of the oceanic crust. At smaller source-to-receiver ranges, there is a refracted phase with an apparent phase velocity of ~7 km/s, and it is often associated with a prominent reflection-like arrival (Figure 5). Given its apparent velocity, we refer to the refraction as *P3*, and therefore the reflection is referred to as *P3P* (Figures 5b and 5c). *P3*, with increasing range, leads into a *P3-PmP-Pn* junction as would be expected for a layer of oceanic crust located beneath the volcanic edifice. The *P3P* phase is unexpected, since reflections or strong triplications are not generally observed at the top of layer 3 in oceanic crust away from the Hawaiian Ridge. Nevertheless, the presence of the *P3P* and *P3* phases indicate a relatively abrupt transition in velocity with depth from values less than 7 km/s to those of about 7 km/s. One could consider *P3P* to be the extension of *P2P* beneath the edifice. However, an equivalent to a *Pv-P2P-P2* junction is not obvious beneath the edifice (marking the boundary between the overlying edifice, Vp ~5 km/s, and the top of the old oceanic crust, Vp < 6 km/s). In addition, some records do show what appears to be a *P2*-like phase (not modelled in the tomographic inversion) with an apparent wave speed of 5-5.5 km/s that forms a *P2-P3P-P3* junction (Figure 5c), but not all records show this phase. This could be because seismic layer 2 is mostly obliterated by volcanic construction and increased pressure, or that it is mostly obscured by noise and reverberations that appear in the records, or a combination of both. For example, on the north side of station 113 (Figure 5a), where *P2* might be present, the arrival could be confused with a reverberation of the first arrival. For station 119 (Figure 5b), where *P2* might occur, there is no discernible arrival, but station 116 (Figure 5c) does appear to have a *P2* arrival. As will be shown later, the location of the *P3P*/*P3* reflector/transition is consistent with the top of oceanic layer 3. It is possible that there is a smooth lateral transition from the *P2P* reflector to the *P3P* reflector, as might occur if geologic processes increasingly have destroyed the top of the oceanic crust, because the timing of these arrivals does not suggest a step change in depth between the two as the center of the edifice is approached from either side. *PvP*, *P2P*, and *P3P* are considered to be a reflection-type arrival, as is common, but we should keep in mind that they may represent a more transitional change in V*p* with depth, rather than a sharp interface.

Figure 6 shows the travel time data for all stations and seismic phases used in the analysis. One can see the obvious presence of the *Pv* phase beneath the Hawaiian Ridge, as well as an increase in the time and range to cross-over points of refractions and the positions of reflections from the top and bottom of the oceanic crust, as the station position approaches the Hawaiian Ridge. This indicates downward flexure of the oceanic crust beneath the moat and ridge.

4. Gravity Data

Gravity data were acquired during the cruise of R/V *Marcus G. Langseth* (Cruise MGL 1806) with an axially-constrained Bell Aerospace BGM-3 sensor mounted on a gyrostabilized platform. In June 2018, the sensor was replaced and the instrument recalibrated with a new pulse rate count to mGal conversion factor of 5.096606269 mGal/count and bias of 852,513.49 mGal using tie-in data between the BGM-3 sensor and the Honolulu Alpha absolute gravity station. Tie- in data since June 2018 indicate the new sensor system has performed well with a mistie at the start of MGL1806 (some 90 days later) of -5.2 mGal and a relatively small drift rate during the cruise of +0.155 mGal/day (Watts et al., 2020).

Prior to correcting for latitude and the Eötvös effect the drift corrected BGM-3 1 s count data were filtered with a 120 s Gaussian filter (as recommended by the manufacturer), to remove accelerations due to ship motions. While such a filter is highly effective at removing swell “noise”, Watts et al. (2020) found there was still significant noise at high frequencies (short periods), albeit with much less power than the swell “noise”. We therefore applied a second filtering step using a Gaussian filter (width = 1.0 km), which significantly reduced the high frequency noise and extended the range of the overall decrease in power with increasing frequency in the spectral data at low frequencies.

5. Tomographic Imaging

Tomographic images were constructed using the travel-time data and the iterative tomographic method of Dunn et al. (2005), which includes a three-dimensional forward problem to compute ray paths and travel times for a starting model, and an inverse problem to construct the tomographic image from the difference between observed and calculated times. The method allows for a single reflection surface, which was employed separately for the different types of reflection data, as discussed below.

Similar to Xu et al. (2022), the analysis employed a Monte Carlo approach, and was carried out in stages, with each stage consisting of the solution of 75 models, from which an average 'final' model is computed, and the standard deviation of image values about that mean model provides an estimate of the model's relative uncertainty. In the first stage, the primary refractions (*P1*, *Pv*, *P2*, *P3*) were used to solve for crustal and edifice structure. In this step, a shallow reflector was not included, because preliminary work showed that with a thin sediment layer, complicated geology, and the wide station spacing, including a reflection for the base of the sediments complicated the shallow-most *P*-wave velocity imaging.

In the second stage, the final model from stage one provided a base starting model, a reflection surface was added to the model parameterization, and the *P2P* and sub-edifice *P3P*, *P3* data were included in the inversion. The reflector/refractor that gives rise to the *P2P*/*P2* data and the reflector/refractor that gives rise to the *P3P*/*P3* data beneath the edifice were modeled as a continuous feature. Despite that they probably represent different lithologic contacts, they appear to be continuous in the records, and a continuous feature fits the overall data. Therefore, the goal was to compute a smooth 'mean' estimate for the position of a continuous reflector beneath the Cretaceous seamounts, and the Hawaiian Ridge. Yet, with the 15-km-wide station spacing, and given data uncertainties, we cannot rule out some sort of step discontinuity between the two features. The origin of these features is discussed more below. In the third stage, the result from the prior stage was used as a starting base model, a reflector was included to represent the Moho, and the phases *P1*, *Pv*, *P2*, *P3*, *PmP*, *Pn* were included. Again, a stack of models was calculated and the mean image and its standard deviation were computed.

The final image is shown in Figure 7 and the estimate of image uncertainty is shown in Figure 8. While this is not a true model uncertainty, it gives some idea of the relative variation in uncertainty across the image. It is also useful to keep in mind that the model uncertainty is tied to a particular parameterization and choice of regularization constraints. For example, if each solution had been allowed to be less smooth, then the set of all solutions would have more variance and the model uncertainty estimate would be greater; when we allow more degrees of freedom in the solution, the individual parts of the solution become less certain, a well understood aspect of parameter estimation problems. The approach taken here, was to solve for the smoothest solutions that fit the data, which tends to reduce model variance and the estimate of the uncertainty of the final solution. The χ^2-misft of the final model is 1.1. Residual statistics can be found in the Supporting Information (Figure S2).

6. Gravity Modelling

To verify the final seismic tomographic image, we computed the gravity effect of the seismically constrained crust and mantle structure assuming different empirical relationships between *P* wave velocity and density and comparing them to the observed free-air gravity anomaly. Figure 9 shows the iso-velocity contours derived from Figure 7a, the density structure assumed in the gravity calculations and the observed and calculated gravity anomalies along Line 01. The observed gravity anomaly data was acquired while R/V *Marcus G. Langseth* was shooting the OBS profile and is based on the 1 s BGM-3 count data and Gaussian filter widths of 120 s (grey dots, Figure 9a) and 1.0 km (red solid line, Figure 9a). The calculated gravity anomaly assumes a layered structure in which the density contrast between layers is derived from the average *P* wave velocity above and below an iso-velocity contour. Figure 9a (dark blue solid line) shows the sum of the gravity effect of all the layers, which was computed using a 3D Fast Fourier Transform modelling method for the seafloor bathymetry, a 2D line-integral method for each sub-seafloor layer and an empirical relationship between *P* wave velocity and density defined by Gardner for $1.5 < V_p < 6.1$ km/s and Nafe-Drake for $V_p >= 6.1$ km/s (Brocher, 2005). The contributions of the gravity effect of the bathymetry and individual sub-seafloor layers to the sum are given in Supporting Information (Figure S3). A similar gravity modelling approach was used successfully to verify seismic imaging of crustal and upper mantle structure in the Emperor Seamount chain (Watts et al., 2021; Xu et al, 2022).

We selected the Gardner and Nafe-Drake empirical relationships because it yielded the best Root Mean Square (RMS) difference between the observed and calculated gravity anomaly (12.8 mGal). Other relationships tested were Nafe-Drake and Nafe-Drake and Christenson (dashed dark blue lines in Figure 9a) but these yielded a significantly higher RMS difference between the observed and calculated gravity anomaly of 18.1 and 24.3 mGal respectively. The main difficulties with these relationships were their inability to account for the amplitude of the free-air gravity anomaly highs over Māhukona and Kohala volcanoes that extend to the northeast of Hawai‘i, although they performed better over the Hāna Ridge that extends to the southeast of Maui. They also improved on the Gardner and Nafe-Drake empirical relationship in the flexural moat to the south of Hawaiʻi, including over the crests of the Cook and Jaggar seamounts.

We conclude that the gravity analysis verifies the seismic tomographic model. Significantly, no adjustments had to be made to the seismic tomographic model of the crust or mantle velocity structure to fit the observed gravity data. The main discrepancies that remain are in the amplitude of the gravity high, which is underpredicted by up to ~18 mGal over the extension of the Māhukona volcano and up ~10 mGal over the extension of the Kohala volcano. We speculate these discrepancies are most likely due to lateral changes in density within the shallow carbonate layers that comprise the submarine terraces in this region. The smaller discrepancies over the Hāna Ridge may be due at least in part to 3D effects associated with the high wave-speed interior and, hence, dense body that underlies this region. Other discrepancies are in the flexural moat southwest of Māhukona but these may be attributed to regional differences in the empirical relationships between *P* wave velocity and density between, for example, that of the edifice region and the flanking flexural moats.

7. Flexure modelling

One of the aims of this paper has been to use the seismic refraction technique to constrain the internal seismic velocity and, hence, density structure of the volcanic loads that comprise the southeastern end of the Hawaiian Ridge and the manner that the Pacific oceanic plate has responded to these loads. Refraction data show, for example, that the northwest flank of the Hawaiʻi edifice is associated with *P* wave velocities of 4.5-6.5 km/s (Figure 7a), which correspond to average densities of 2513-2773 kg/m^3 according to the empirical velocity-density relationships of Gardner and Nafe-Drake. The southeast flank, in contrast is associated with a shallow high velocity core (>7.0 km/s) (Park et al., 2009), which implies densities of >2968 kg/m^3. A similar high velocity and density core is associated with the volcanic rift extension of the Maui edifice (Figure 7a) and has been discovered at Jimmu guyot in the Emperor Seamount chain (Watts et al., 2021; Xu et al., 2022). Moreover, refraction data show that the Hawaiʻi edifice is associated with a depression of the Moho of up to 6-6.5 km: the largest depression associated with the Moho that has yet been imaged along the Hawaiian-Emperor Seamount Chain (Figure 7). The depression is greatest beneath the edifice and extends several tens of km beyond the edifice, suggesting that it represents the flexural response of the interior of the Pacific plate to relatively young (<~450 ka) volcano loading.

To evaluate the contribution of plate flexure to the seismically constrained crustal structure we compared the iso-velocity contours, the possible top of oceanic crust (Figure 7b), the upper reflector depth based on the *P2P* and *P3P* phases (Figure 7a), and the lower reflector that defines the bottom of oceanic crust (i.e., Moho) to the calculated depths based on 3D elastic plate (flexure) models. We assume for simplicity that the present-day seismic structure is the cumulative result of flexure due to three main loads: the Cretaceous seamount province southwest of Hawai'i, the relatively old (2-5 Ma) islands between Kaua‘i in the west and Maui in the east, and the relatively young (<~0.45 Ma) island of Hawai‘i (Figure 10).

The flexure was modelled assuming different values of the average load, average infill and mantle densities and flexural rigidity and equivalent elastic thickness, T_e. Initially, the same set of parameters was used for all three loads as had been derived by optimal minimization (Cilli et al., 2023) from reprocessed *R/V Robert D. Conrad* MCS data acquired in the vicinity of O‘ahu (i.e., average load density = 2737 kg/m^3, average infill density = 2701 kg/m^3, mantle density = 3300 kg/m^3 and T_e = 26.7 km). The resulting RMS difference between observed and calculated possible top of oceanic crust and the upper and lower seismic reflector positions (Figure 7) were 1.1 km, 0.9 km, and 0.7 km respectively (Model 1, Table 2). We then reduced the T_e in the Cretaceous seamount province to 3 km, which is within the 2-6 km range expected for bathymetric features that form at or near the fast-spreading East Pacific Rise (Cochran, 1979). The resulting RMS for the possible top of oceanic crust was similar, but the RMS for the Moho reflector positions decreased slightly to 0.6 km (Model 2, Table 2).

The flexure for Model 2 (Table 2), which is shown in profile form in Figure 9 by the light blue shaded region and the light blue solid line and in plan form in Figure 10, is a satisfactory visual fit to both the seismic and gravity observations. In particular, the model accounts for the depression of the crust in the Cretaceous seamount province, the amplitude of the free-air gravity anomaly over the Hawai‘i edifice and the wavelength of the free-air gravity anomaly over the flanking moats. The maximum cumulative flexure along Line 01 is 6.23 km, which is made up of a contribution of 0.39 km (i.e., 6.3% of the total flexure) from the Cook and Jaggar seamounts, 2.66 km (42.7%) from Maui and older islands in the Hawaiian Ridge, and 3.18 km (51.0%) from Hawai‘i.

The main discrepancies are the top of oceanic crust is overpredicted in a wide region that extends from the southwest flank of Hawai‘i, across the flexural moat, almost to the bulge, and the Moho depth is underpredicted beneath the Kohala Canyon region and overpredicted beneath the southwest flank of Hawai‘i. We assumed in Figure 9 that the pre-flexure average thickness of the oceanic crust is 4.4± 0.9 km based on the mean difference between the upper and lower reflectors. The thickness increases to 4.7±1.4 km if we use the possible depth to top of oceanic crust (Figure 7b) instead of the upper reflector. One possibility therefore is that the oceanic crust is thicker south of the Hawaiian Ridge than it is to the north since it is unaffected by the MFZ system. A thicker crust, for example by 1.5 km, could explain the discrepancy. The discrepancies in Moho depth are more localized and therefore difficult to reconcile. They could be caused by differences in elastic parameters such as the elastic thickness, T_e. However, decreasing T_e to ≤ 20 km at Hawai‘i (i.e., Models 3 and 4, Table 2) or increasing T_e to ≥ 40 km at Hawai‘i (i.e., Models 6 and 7, Table 2) appear to make the fit between observed and calculated Moho worse.

To investigate this further we computed the free-air gravity anomaly for different values of the elastic thickness and compared them to the observed anomaly. We first assumed a simple ‘object-oriented’ model in which the main contribution to the gravity anomaly along Line 01 was given by the load of Hawai‘i and its flexural compensation. The RMS difference between the observed and calculated gravity for T_e = 26.7 km (i.e., Models 1 and 2, Table 2) is 15.3 mGal and increases significantly for T_e ≤ 20 km (i.e., Models 3 and 4, Table 2) and T_e ≥ 40 km (i.e., Models 6 and 7, Table 2), consistent with the results from cumulative Moho flexure modelling. We note here that the RMS difference between the observed and calculated gravity for Model 5 in Table 2 where T_e = 30 km at Hawai‘i is only 1.7 mGal higher than that for Model 2, yet the Moho depth (and the possible depth to top of oceanic crust) fit equally well as Model 2.

We have so far assumed in the flexure modelling an average load density of 2737 kg/m^3. As several studies have shown (e.g., Lambeck, 1981; Minshull & Charvis, 2001; Watts, 2001), both the flexure and gravity anomaly associated with volcano loading depend on the assumed load density. We found, however, that changing load density within an acceptable range (i.e., 2587–2887 kg/m^3) had only a small effect on the flexure and gravity anomaly (Figure 9a). This is because increasing the load density increases the amplitude of flexure and its associated gravity “low” but increases the gravity “high” so the net effect on the gravity anomaly is small. Nevertheless, a load density higher than 2737 kg/m^3 could be justified on the basis that a larger proportion of the east flank of Hawaiʻi is underlain by high *P* wave velocity, and hence denser mafic and ultramafic rocks, than the southwest flank and that it helps to explain the Moho discrepancy on Line 01, at least the one associated with the region beneath the Kohala Canyon.

8. Seismic Results

8.1 Oceanic crust and mantle structure

Away from the complexities of the Cretaceous Seamounts, the Hawaiian Ridge, and the most anomalous parts of the MFZ, the crust has a typical V*p* profile for Pacific oceanic crust (profile A in Figure 11), with a thin sub-seafloor low-velocity layer (<4 km/s; seismic layer 1) typical of accumulated sediments, a thicker low-velocity layer (4-6.5 km/s; seismic layer 2), usually thought to be the oceanic upper crust and composed of dikes and relatively porous lava flows, a deeper high-velocity layer (~6.5-7 km/s; seismic layer 3), usually thought to be the lower oceanic crust and composed of intrusive gabbroic rocks, and an upper mantle with relatively modest lateral changes in V*p* from ~7.85 to 8.1 km/s. The boundary between the crust and mantle, or Moho, is generally marked by a clear reflection (Figures 3, 5, 7), and the average crustal thickness away from the edifice and fracture zone, ~6 km, is typical of oceanic crust formed at faster spreading rates.

The upper reflector in Figure 7 is more difficult to interpret. In the moats flanking the Hawaiian Ridge, this reflector generally marks a velocity contrast between low velocities above, as would be expected for sediment infill, and higher-velocity oceanic crust below. However, the upper reflector is below the base of low velocities consistent with volcaniclastic sediments (e.g., Hammer et al., 1994; Weigel & Grevemeyer, 1999), suggesting it could represent a deeper structure below the moats, such as the top of seismic layer 2B (e.g., Carlson, 2018; Christeson et al., 2019). Alternatively, the reflector position may simply be biased deeper due to imaging and resolution constraints. Either is possible, since the large water depths, the thinness of the sediment layer, and the wide OBS spacing, taken together, make it difficult to properly determine the depth of this feature and what it represents. Irrespective, away from the Cretaceous Seamounts and Hawaiian Ridge, the upper reflector does appear to smoothly follow the expected base of a sedimentary layer, even if it were to be a deeper seismic horizon.

In order to estimate the sediment thickness in the flexural moats, we consider the base of the upper low-velocity layer (i.e., the 4 km/s contour) as a lower bound, and the upper reflector position as an upper bound. When compared to the seismically-constrained thickness of sediments along older segments of the Hawaiian-Emperor Seamount Chain (Watts et al., 2021; Xu et al., 2022), the moat sediments along Line 01 are relatively thin (<1-1.5 km), except in the basins formed between the seamounts and the Hawaiian Ridge where they are up to ~2.5 km thick. It is expected that over the past ∼100 Myr only about 0.1 km of the sediment formed due to background pelagic sedimentation (Olson et al., 2016). Therefore, a large fraction of the moat infill is likely due to the deposition of volcaniclastic sediments, including mass-wasting products derived from the flank collapse of the Hawaiian Ridge. Since moat sediments are largely composed of debris flows, we can conclude that sufficient time has not passed for this process to fill the moat, especially on the north side of the seismic line, as it has along older sections of the ridge. On the south side, the thicker sediments filling the region between the volcanic edifice and the seamounts may be largely related to the Alika I and II debris avalanches (Lipman et al., 1988).

8.2 Molokai Fracture Zone (MFZ)

The crust in the area of the MFZ system, which extends southwards from the northern part of Line 01 to at least the Hāna Ridge, is generally less than 5 km thick (Figure 7a and profiles E and F in Figure 10). Locally thin crust (~3.5 km) is found beneath a topographic ridge located between two fracture zone lineaments (between stations 130 and 131; Figure 4b). Here, *PmP* reflections are difficult to identify and rather tenuous, but the transition from crustal velocities to mantle velocities at short offsets is obvious and nevertheless indicative of thin crust. To either side of this ridge, low velocities penetrate deep into the lower crust (Figure 7a).

Broadly speaking, thinner oceanic crust and anomalous velocities are often associated with fracture zone offsets (e.g., Detrick et al., 1993; Detrick & Purdy, 1980; Minshull et al., 1991; White et al., 1984), but not always (e.g., Davy et al., 2020; Growe et al., 2021; Marjanović et al., 2020). Thinner crust is usually attributed to suppressed mantle thermal and upwelling effects along the portions of mid-ocean ridges where the offsets were actively slipping as transform faults (e.g., Detrick et al., 1993; Stroup & Fox, 1981; White et al., 1984). In the study area, where there are several offsets, it is conceivable that similar processes may be important.

8.3 Hāna Ridge

The Hāna Ridge is a volcanic rift extension from the Haleakalā shield volcano of East Maui, which is assumed to be similar in age to the shield at ~1.0-1.2 Ma (e.g., Chen et al., 1991; Faichney et al., 2010; Taylor, 2019). Its subsurface structure is dominated by a high-velocity (>6.5 km/s) and density core that extends upward from what would have been the top of the original oceanic crust, to shallow (~1.5 km) depth below the seafloor (Figure 7a; profile D in Figure 10). Over the Hāna Ridge, the capping low-velocity (<4 km/s) layer is up to ~2-3 km thick, and is laterally variable such that the thinnest part overlies the high-velocity core. Beneath the interior core material, there is no clear velocity discontinuity between it and the top of the oceanic crust. The velocity structure suggests the core is made up of a mix of mafic feeder dikes, lava flows, and frozen mush zones with variable amounts of olivine cumulates (e.g., Hammer et al., 1994; Houtz & Ewing, 1976; Weigel & Grevemeyer, 1999).

Our seismic line crosses the morphologically smooth western section of the Hāna Ridge, whose surface displays a series of former shoreline terraces, indicating it was once at or near sea level (Clague et al., 2000; Moore et al., 1990; Ren et al., 2006). The terraces have subsided due to further growth of the Hawaiian Ridge, and they are generally tilted toward the center of Hawaiʻi (Moore et al., 1990). Available dredge samples from the summit of the Hāna Ridge, in the area of the seismic line, are largely composed of basaltic flows, volcaniclastic and hyaloclastite materials, coral reefs and very little sediments (e.g., Eakins & Robinson, 2006; Hanyu et al., 2007; Hein et al., 1996; Moore et al., 1990; Ren et al., 2004). Hence, we suggest that the shallow low-velocity layer is largely comprised of highly porous volcanic materials (e.g., lava flows, dikes, and volcanoclastic and clastic debris) and a small percentage of corals and sediment. The edges of the Hāna Ridge, also draped by low velocities, are probably high-porosity lava flows (e.g., Eakins & Robinson, 2006; Moore et al., 1990), and debris flow material clinging to the slopes (e.g., Eakins & Robinson, 2006; Smith et al., 2002).

8.4 Hawaiʻi Island: Māhukona and Kohala volcanoes

The seismic line crosses the western submarine flank of the island of Hawaiʻi, which, in this location, is composed of two shield volcanoes, Māhukona and Kohala (Figure 2). Here, the shallow seismic structure reveals a thin (generally <500 m) capping low-velocity (<3.5 km/s) layer followed by a thicker (~0.9-1.8 km) layer with velocities of 3.5-4.5 km/s (Figure 7a). Although these upper layers are generally not well-resolved in tomographic images, the use of the MCS shot data herein helps provide better constraints, and we see some layer thickness variations across both Hawai‘i Island and Hāna Ridge and the region in between. The topographic saddle (Kohala Canyon) located between the Hawaiian edifice and Hāna Ridge is directly underlain by a thick low-velocity region, that suggests more than 1 km of accumulated debris infill. The velocity contours also show layer thickness variations across Hawai‘i that suggest a saddle-like divide between Māhukona and Kohala structures, located at positions -40 to -23 km along the seismic line. Note that the gravity profile also indicates a prominent saddle in the density layers of the upper edifice (Figure 9). Models of the gravity structure based on the tomographic image tend to underpredict the gravity saddle, suggesting the tomographic image may under-represent the structural divide beneath the two volcanic masses.

The seismic structure of the main body of the flank of Hawai‘i is associated with V*p* velocities of ~4.5-6.5 km/s, with a general increase in velocity with depth (Figure 7a). Compared to neighboring values at the same depth, there are slightly lower velocities down the middle of the edifice, roughly located beneath the shallow saddle. This is not a well-resolved structure, but appears to separate the seaward extension of the flanks of Māhukona and Kohala. There is also a weak velocity inversion from ~2-4 km depth below the seafloor that extends over a ~50-km-wide region beneath the saddle region (Figure 7a). This feature is controlled by a variety of seismic phases passing through the area, including *Pv*, *P3P*, *P3*, *PmP*, and *Pn*. Seismic wave amplitudes are sensitive to gradients, and for stations with *Pv* energy that turns in this region, the observed *Pv* amplitudes die out with range (Figures 5b and 5c), providing additional evidence for a negative, or nearly negative, velocity gradient with depth. We interpret this portion of Hawai‘i to be comprised largely of extrusive volcanic materials and debris flows formed during shield building, as expected from available drilling data on the island (holes HSDP-1 and HSDP-2 of Hawai‘i Scientific Drilling Project near Hilo; Garcia et al., 2007; Hauri et al., 1996; Moore et al., 1996; Stolper et al., 1996). The burial of this material would be expected to close cracks and pores and increase its wave speed with depth.

The Moho plunges downward beneath the Hawai‘i edifice and Hāna Ridge, and is depressed downward by ~6-7 km over a ~400-500-km-wide region (Figure 7). The upper reflector (red part of the curve in Figure 7a) is also deflected downward. As discussed previously, elsewhere the upper reflector is probably associated with the top of the oceanic crust (black portion of the curve in Figure 7a), but here, beneath the edifice, a reflection from the top of oceanic crust is unconfirmed. Instead, the red portion of the reflector is only ~3.5-4 km above the Moho and appears to mark the top of the lower oceanic crust, not the top of the crust. This is because its height above the Moho is consistent with this horizon, and because high V*p* values indicative of the lower crust are located immediately below. Its position and underlying velocities are largely controlled by the reflection-refraction combination, *P3P-P3* (Figure 5). The refraction *P3* indicates the material below the boundary is consistent with the Pacific lower crust (V*p* >6.5 km/s). There is evidence for an upper-crustal *P2*-like refraction occurring above the boundary (Figure 5c), and forward modeling of this phase is consistent with an upper crustal layer that is up to 2-2.25 km thick above the *P3P* reflector (as indicated by the black dashed curve in Figure 7d). We note that due to resolution constraints, no discontinuity could be determined between the red and black portions of the curve in Figure 7a. Previously, deep reflectors and refractors were discovered beneath Hawaiʻi and were also suggested to mark the top of the lower oceanic crust (Hill, 1969; James & Savage, 1990).

8.5 Cook and Jaggar seamounts

Beneath the Cook and Jaggar seamounts, which are located to the southwest of the Hawaiʻi edifice, the added volcanic material thickens the crust by as much as 5 km, and the top of the mantle, as indicated by the lower reflector, is deflected downward by ~1.5-2 km (Figure 7). Here, the upper reflector also dips downward, approximately paralleling the Moho, and departs from the shallow low-velocity layer, which drapes over the tops of the seamounts. While we do see a reflector near the base of this shallow layer, *PvP* in Figure 3b, it was not modeled in our analysis. Instead, in this area our reflector position is governed by the seismic phase combination, *Pv-P2P-P2*, as seen in Figure 3b, with the idea that the reflector marks the top of the oceanic crust beneath the seamounts. *P2* refractions, from what we regard as the top of oceanic crust, generally have apparent velocities of >5.5-6 km/s, while *Pv* refractions, from what we regard as the interior of the seamount, generally have apparent velocities of <5-6 km/s. This is illustrated in the tomographic image, wherein the seamounts have moderate V*p* interiors (~4.5–6 km/s) resting on deeper material of 6-7 km/s that appears to be the original oceanic crust.

Our interpretation is that, despite their relatively small size, the Cretaceous Cook and Jaggar seamounts are associated with a depression of the crust of 1.5-2 km, over a ~80 km wide zone. The interiors of the seamounts are consistent with a mass of dikes and compacted lava flows, but there are smaller regions beneath the Jaggar and Indianapolis Seamounts with

V*p* values exceeding 6.5 km/s, suggesting intrusive, mafic or ultramafic rocks (Figure 7a). Draped across the seamount interiors, is lower V*p* material (4-5 km/s), possibly representing porous lava flows, which is draped again by even lower V*p* material (2.5-3.5 km/s), which may be a mix of basaltic flows, hyaloclastite breccia, pelagic sediments, and deep-sea corals, examples of which have been either dredged (e.g., Chave et al., 1986; Moore & Clague, 2004) or directly observed via bottom photography (Rowley, 2017).

9. Discussion

9.1 Oceanic crustal and upper mantle structure

Away from the Hawaiian Ridge, the oceanic crust seen along the seismic line displays a mostly typical structure compared to the average Pacific oceanic crust (Figure 10). However, notable deviations occur across the broad Molokai Fracture Zone, where the crust is generally thinner (<5 km), and some individual strands are associated with absent lower oceanic crust sections, and indications of fault-related damage in the form of deep low-velocity regions. The upper mantle has V*p* values of ~7.85 to 8.1 km/s. There are no mantle anomalies associated with the fracture zone damage areas in the crust, but given the narrowness of these features, and the broad resolution at mantle depths, any mantle-level anomalies may not be resolvable.

Narrow topographic ridges, such as the one located between stations 130 and 131 (Figures 4 and 7), are often found located parallel to fracture zone lineaments (e.g., Basile & Allemand, 2002; Chen, 1988; Karson & Dick. 1983). They have been variably described as originating as a consequence of differential thermal subsidence, lateral heat transfer, extension perpendicular to the transform, erosion of a lithospheric plate along the transform boundary producing flexural uplift (e.g., Basile & Allemand, 2002; Chen, 1988; Pockalny et al., 1996; Sandwell & Schubert, 1982), or due to excess volcanism to one side of the original transform offset (e.g., Karson & Dick. 1983; Lonsdale, 1983; McNutt et al., 1989). Given that the narrow ridge is associated with anomalously thin crust, this suggests that it formed in response to plate boundary stresses and uplift, rather than as a constructional feature. To either side of this ridge, the deep, anomalously-low crustal velocities suggest regions of intense fracturing and alteration associated with fracture zone strands that pass through these areas.

Beneath the edifices of the Hawaiian Ridge, the state of the upper oceanic crust is uncertain (Figure 7). A few stations (e.g., Figure 5c) indicate an upper crustal layer sandwiched between the edifice and the lower oceanic crust (Figure 7b). One possibility is that due to its thinness, it is difficult to detect via the experiment geometry. An alternative explanation is that oceanic layer 2 is compressed or overprinted enough to achieve near-edifice-like velocities and lack a sharp enough transition to produce clear reflections. Perhaps both of these possibilities are true to some extent.

Since the flank of the Hawaiʻi edifice is not expected to be characterized by significant amounts of melt flow through the oceanic crust, we do not expect the upper oceanic crust was destroyed by such melts, as has been revealed at Jimmu guyot in the Emperor Seamounts (Watts et al., 2021; Xu et al., 2022). Likewise, the lower oceanic crust and mantle are not highly variable (Figure 7), suggesting little overprinting by new material rising from a melt region below. The Hāna Ridge has a prominent high velocity core, but the lavas are expected to have flowed laterally from Haleakalā down the rift system at shallow levels, rather than intrude old oceanic crust or mantle.

There is some indication of slightly lower V*p* values in the mantle beneath the edifice area and beneath Indianapolis Seamount (Figure 7a). However, neither the tomographic image nor the record sections indicate a large-scale sub-Moho layer of low V*p* values, mid-range between crustal and mantle values, as might be expected for wide-spread crustal underplating of volcano-related magma as previously suggested for several other intraplate volcanoes and the Hawaiian Ridge (e.g., Leahy et al., 2010; Park & Rye, 2019; ten Brink & Brocher, 1987; Watts et al., 1985). With the seismic line not crossing any major centers of mantle melt supply, one possibility is that crustal underplating, if it exists, is localized to mantle feeder zones.

9.2 Volcano structure

Hawaiian Ridge volcanos grow over long-time spans and overlap each other both physically and in age. Māhukona is the smaller and older of the two Hawaiʻi Island volcanos, while Kohala is larger and younger and at the surface overlaps the Māhukona edifice (Figures 2 and 7). Māhukona ended its shield and post-shield growth ~0.4 Ma, and Kohala began its growth ~1 Ma, indicating that there appears to have been ~0.6 Myr of overlap in their growth (Clague & Moore, 1991; Lipman & Calvert, 2011; Sherrod et al., 2007). The summit of Māhukona was once ~250 m above sea level, but has since subsided below sea level, starting between 435,000 and 365,000 years ago (Clague & Moore, 1991). Kohala was believed to have breached sea level more than 500,000 years ago (Campbell, 1984). Along the cross-section of the seismic line, Kohala's growth may have been initially buttressed by Māhukona to the south and the Hāna Ridge (~1.0-1.2 Ma) to the North.

Seafloor topography, acoustic backscatter maps, and available dredge samples (Clague & Moore, 1991; Garcia et al., 2012; Huang et al., 2009; Smith et al., 2002) suggest there is a large carbonate platform extending across the shallow-water part of the edifice flank, covering part of both Māhukona and Kohala volcanos, whose contact lies somewhere beneath. Hence, we suggest that most of the shallow low-velocity layer is largely comprised of a mixture of carbonate and volcanic materials (e.g., reef material, carbonate cement, lava flows, dikes, and volcanoclastic and clastic debris) (Figure 7). The edges of the edifice are also overlain by low velocities, which could indicate high-porosity lava flows (Staudigel & Schmincke, 1984), but is also consistent with debris flow material clinging to the slopes (e.g., Smith et al., 2002).

In the tomographic image, Māhukona and Kohala volcanos generally appear as a single entity, but the saddle in the gravity data and low-velocity layers, the slightly lower V*p* values below this feature, and a neighboring inflection in the contour lines of the edifice topography all suggest a possible boundary between the two (Figure 7). The seismic saddle could have been a topographic saddle between the volcanoes that subsequently filled with volcaniclastic debris, Kohala lava flows, and other material. Garcia et al. (2012), on the basis of seafloor topography and rock geochemistry, also place the contact between Māhukona and Kohala in this location. Figure 7b indicates the possible relative locations of Māhukona, Kohala, and Hāna structures along the seismic line. Together they act to depress the oceanic crust by up to 6-7 km over a ~400-500-km-wide region. These features have added up to 13 km of material to the oceanic crust, or 1800 km^3/km (volume per kilometer along the ridge); ~30% of which rises above the surrounding seafloor, and 70% rests in the depression.

The central conduit of Kohala volcano is thought to be located subaerially to the east of the seismic line, and there is no known volcanic rift or gravity anomaly extending outward from the conduit area across the seismic line. The location of the central conduit of Māhukona is unknown. Clague and Moore (1991) suggested it is located beneath the carbonate platform on the shallower portion of the edifice, near station 116 of our seismic line (Figure 2). We find no strong high-V*p*, high density feature in this area, as is observed beneath the Hāna Ridge (Figure 7a) and other submarine volcanoes (e.g., Contreras-Reyes et al., 2010; Hammer et al., 1994; Staudigel & Schmincke, 1984; Watts et al., 2021; Weigel & Grevemeyer, 1999; Xu et al., 2022). Alternatively, Garcia et al. (2012) suggest the central conduit is located to the northwest of our seismic line, and they found a weak elongate residual gravity anomaly (indicating denser subsurface material) that crosses the seismic line between stations 113 and 114 (Figure 2). In this area there is some indication of higher V*p* values within the edifice (Figure 7a), as compared to either side (4-7 km below the seafloor), but the case for a rift feeder zone in this location is not compelling.

The seismic structure and gravity modelling reveal a high *P*-wave velocity and dense body in the interior of Maui's Hāna Ridge, with velocities and densities >7 km/s and 2900 kg/m^3. Similar bodies have been described by Park et al. (2009) and Flinders et al. (2013) elsewhere in Hawai‘i, and by Watts et al. (2021) and Xu et al. (2022) at Jimmu guyot in the Emperor Seamount chain, where they have also been interpreted as intrusive rocks of mafic and ultramafic composition. Since melts are largely expected to have been fed laterally beneath the ridge from Haleakalā volcano (East Maui), the core's triangle shape may be a consequence of a process wherein older material is wedged outward as new material is intruded over time, rather than indicative of a broad supply zone that narrows upwards. The suggested intrusive nature of the core implies relatively long residence times and slow cooling in melt/mush zones formed by these lavas. The fate of the top of the pre-existing oceanic crust during this process is unknown. Its low-V*p* volcanic layer may have been compacted, squeezing out pore space, by the overburden pressure of the Hawaiian Ridge volcanics. Additionally, it may have been overprinted by new material that intruded this region.

9.3 Plate flexure

The flexure calculations in Figures 9 and 10 are based on a continuous elastic plate with a uniform thickness. We have therefore not considered the possibility that T_e varies spatially along Line 01 or that the plate might be discontinuous or broken (e.g., Klein, 2016; Manríquez et al., 2014). While we cannot rule out lateral changes in T_e, they are not required to explain either the observed seismic reflectors or free-air gravity anomaly. A local decrease in T_e beneath Hawai‘i, for example, would help explain the seismically constrained depth of Moho but it would decrease the amplitude and wavelength of the calculated free-air gravity anomaly and make the fit to the observed gravity worse. Moreover, a broken plate is not required to explain either the reflector depths to the top and base of the oceanic crust or the free-air gravity anomaly. In fact, the reflector depths in Figure 7 reveal a remarkably continuous concave up flexure beneath the main center of mass of the edifice along Line 01 and there is no evidence in the seismic data for either a broken plate or a concave down flexure.

A possible criticism of our gravity modelling thus far is that there is an inconsistency in the way the cumulative flexure and the gravity anomaly have been calculated. The cumulative flexure along Line 01 has been calculated by summing the flexures caused by each set of loads in the Hawaiian Ridge region (e.g., Figure 10) while the gravity anomaly has been calculated assuming that only the load of Hawaiʻi and its flexural compensation contributes to the gravity anomaly and that the compensation of the older island loads (i.e., Maui to Kaua'i) and the Cretaceous seamount province contribute. While this is the case for the Cretaceous seamount province it is not for the older island loads. Hawaiʻi, for example, is in the flexural moat of Maui and the older islands.

The problem can be addressed by 'process-oriented' rather than 'object-oriented' gravity modelling. In such an approach a gravity anomaly measured at the present day is considered the sum of all the geological processes that have formed a bathymetric/topographic feature (e.g., Watts, 2018). In the case of a rifted continental margin, for example, these processes include crustal thinning at the time of rifting, syn-rift and post-rift sedimentation and in some settings, erosion. Figure S4 in Supplementary Information shows that a process-oriented approach in which the observed gravity anomaly along Line 01 is considered the sum of the individual anomalies associated with the volcano loading and its flexural compensation, first at the Cretaceous seamount province (T_e = 3km), then at the islands between Maui and Kaua'i (T_e = 26.7 km), and finally at Hawaiʻi (T_e = 26.7 km), can generally explain the amplitude and wavelength of the observed gravity anomaly. Tests using a 'process-oriented' approach (Figure S4 in Supplementary Information) generally confirm the results summarized in Table 2 in that they show T_e significantly lower and higher than 26.7 km at Hawaiʻi can be ruled out because they predict too short a wavelength and low an amplitude and too long a wavelength and high an amplitude respectively to explain the observed gravity anomaly.

Irrespective, we recognize that the seismic and gravity data used in this study may provide only a 'snapshot' of the deformation in what is a dynamically evolving volcano loading and flexing system. Tide gauge, historical and archaeological data suggest Hawaiʻi has been subsiding relative to other islands in the Hawaiian Ridge at a rate of >1 mm/yr (e.g., Moore, 1970). The deformation measured along Line 01 mainly reflects the flexure caused by Maui and older islands as well as the nearby volcanoes of Kīlauea, Mauna Loa and Mauna Kea on Hawaiʻi, which are <450 ka in age (e.g., Moore & Clague, 1992). While Maui is 2-3 Ma and so should be compensated, Hawaiʻi is younger and so may not have reached a state of isostatic equilibrium yet. Indeed, Watts & ten Brink (1989) used a 'object oriented' gravity modelling approach and free-air gravity anomaly and bathymetry profiles of the flexural moat and bulge and an elastic plate model to derive a best fit T_e = 40 km for the eastern flank of Hawaiʻi, which is significantly higher than the T_e = 26.7 km deduced on seismic Line 01 of the western flank of Hawaiʻi. Zhong and Watts (2013) subsequently used a two-layer viscoelastic model with a 30 km thick, effectively elastic, upper and lower layer of viscosity of 10^{27} and 10^{21} Pa s respectively to show that Hawaiʻi has undergone as much as ~1.5 km of load-induced subsidence during the past 450 ka. We attribute the higher T_e and the subsidence to incomplete isostatic compensation as the lithosphere at Hawai'i relaxes in its response to volcano loading from its short-term seismic thickness to its long-term elastic thickness.

10. Conclusions

Wide-angle seismic refraction and reflection data, along with gravity data, have revealed the *P* wave velocity and density structure of the crust and upper mantle beneath the northwestern flank of Hawaiʻi, the southeastern flank of Maui, and the ʻAlenuihāhā Channel that separates the two islands. This work reveals the nature of intraplate volcanic loads associated with the Hawaiian Ridge, and the associated lithospheric flexures.

- The seismic structure and gravity modelling reveal a high *P*-wave velocity and dense body with velocities and densities >7 km/s and 2900 kg/m^3 in the core of the Hāna Ridge. We suggest this feature formed from lavas propagating laterally from Haleakalā down the rift system and is comprised of intrusive rocks of mafic or ultramafic composition.
- The northwest flank of the edifice of Hawaiʻi, in contrast, is characterized by lower velocities and densities, which are interpreted as extrusive lavas and volcanoclastic sediments.
- Seismic reflectors at the top of oceanic crust and Moho suggest the pre-existing Pacific oceanic crust at Hawaiʻi is ~4.5-6 km thick, and has been flexed downwards beneath the edifices by up to ~6-7 km below the expected depths of the Hawaiian mid-plate swell crest.

- Across the broad set of lineaments of the Molokaʻi Fracture Zone, the oceanic crust is generally thinner (4.5-5.5 km) and some lineaments are associated with missing lower oceanic crust and deep low-velocity regions suggestive of fault damage to the crust.
- Although there is some indication of slightly lower V*p* values in the mantle beneath the edifice area and beneath Indianapolis Seamount, there is no evidence for significant wide-scale magmatic underplating along the seismic line.
- Simple three-dimensional continuous elastic plate modelling shows that the flexure can be explained by volcano loading in which the Jaggar and Cook seamounts contribute ~6% to the seismically constrained flexure, Maui and the older islands in the Hawaiian Ridge contribute ~43%, and the island of Hawaiʻi ~51%.
- The best fit elastic thickness is 26.7 km, which is similar to values at Maui and the older islands in the Hawaiian Ridge. However, previous gravity and subsidence studies that Hawai'i may still be adjusting to volcanic loading and that isostatic equilibrium is not yet complete.

Acknowledgments

Data used in this research were provided by instruments from the Ocean Bottom Seismic Instrument Center (OBSIC, 2022), which is funded by the National Science Foundation. This research was supported by the National Science Foundation grants OCE-1737243 to R. A. Dunn and OCE-1737245 to D. J. Shillington and A. B. Watts.

Open Research

OBSIC data are archived at the EarthScope Consortium facilities (HI-Emperor, 2019; SAGE, 2023). The cruise data are stored at the Rolling Deck to Repository archive (R^{2}R, 2023). Figures were constructed using GMT 6 (Wessel et al., 2019) and MATLAB (The Mathworks, 2021).

References

Atwater, T., & Menard, H. W. (1970). Magnetic lineations in the northeast Pacific. *Earth and Planetary Science Letters*, *7*(5), 445-450. https://doi.org/10.1016/0012-821X(70)90089-0

Basile, C. & Allemand, P. (2002) Erosion and flexural uplift along transform faults, *Geophysical Journal International*, *151*, 646–653, https://doi.org/10.1046/j.1365-246X.2002.01805.x

Boston, B., Dunn, R. A., Shillington, D. J., Watts, A. B., Gomez de la Pena, L., Grevemeyer, I., et al. (2019). Lithospheric structure across the Hawaiian-Emperor Seamount Chain from seismic wide-angle reflection-refraction tomography. American Geophysical Union, Fall Meeting 2019, Abstract # T43F-0515.

Boston, B., Shillington, D. J., Watts, A. B., Dunn, R. A., Cilli, P., Grevemeyer, I., et al. (2021). The growth and collapse of the Hawaiian-Emperor seamount chain from marine seismic data. American Geophysical Union, Fall Meeting 2021, Abstract #V45B-0130.

Bratt, S. R., & Purdy, G. M. (1984). Structure and variability of oceanic crust on the flanks of the East Pacific Rise between 11 and 13 N. *Journal of Geophysical Research: Solid Earth*, *89*(B7), 6111-6125.

Bridges, N. T. (1997). Characteristics of seamounts near Hawaii as viewed by GLORIA. *Marine geology*, *138*(3-4), 273-301. https://doi.org/10.1016/S0025-3227(96)00114-4

Brocher, T. M. (2005), Empirical relations between elastic wavespeeds and density in the Earth's crust, *Bulletin of the seismological Society of America*, *95*(6), 2081-2092. https://doi.org/10.1785/0120050077

Brocher, T. M., & ten Brink, U. S. (1987). Variations in oceanic layer 2 elastic velocities near Hawaii and their correlation to lithospheric flexure. *Journal of Geophysical Research: Solid Earth*, *92*(B3), 2647-2661. https://doi.org/10.1029/JB092iB03p02647

Campbell, J. F. (1984). Rapid subsidence of Kohala Volcano and its effect on coral reef growth. *Geo-Marine Letters*, *4*, 31-36. https://doi.org/10.1007/BF02237971

Carlson, R. L. (2018). Ocean crustal seismic layer 2C. *Geochemistry, Geophysics, Geosystems*, *19*(9), 3084-3096. https://doi.org/10.1029/2018GC007614

Chave, K. E., Morgan, C. L., & Green, W. J. (1986). A geochemical comparison of manganese oxide deposits of the Hawaiian Archipelago and the deep sea. *Applied geochemistry*, *1*(2), 233-240. https://doi.org/10.1016/0883-2927(86)90007-7

Chen, C. Y., Frey, F. A., Garcia, M. O., Dalrymple, G. B., & Hart, S. R. (1991). The tholeiite to alkalic basalt transition at Haleakala Volcano, Maui, Hawaii. *Contributions to Mineralogy and Petrology*, *106*, 183-200. https://doi.org/10.1007/BF00306433

Chen, Y. (1988). Thermal model of oceanic transform faults. *Journal of Geophysical Research: Solid Earth*, *93*(B8), 8839-8851. https://doi.org/10.1029/JB093iB08p08839

Christeson, G. L., Goff, J. A., & Reece, R. S. (2019), Synthesis of oceanic crustal structure from two-dimensional seismic profiles, *Reviews of Geophysics*, *57*(2), 504-529. https://doi.org/10.1029/2019RG000641

Cilli, P., Watts, A. B., Boston, B., & Shillington, D. J. (2023), Re-processing of legacy seismic reflection profile data and its implications for plate flexure in the vicinity of the Hawaiian Islands. *Journal of Geophysical Research: Solid Earth*. https://doi.org/10.1029/2023JB026577

Clague, D. A., & Moore, J. G. (1991). Geology and petrology of Mahukona volcano, Hawaii. *Bulletin of Volcanology*, *53*, 159-172. https://doi.org/10.1007/BF00301227

Clague, D. A., Moore, J. G., & Reynolds, J. R. (2000). Formation of submarine flat-topped volcanic cones in Hawaii. *Bulletin of Volcanology*, *62*, 214-233. https://doi.org/10.1007/s004450000088

Cochran, J. R. (1979). An analysis of isostasy in the world's oceans: 2. Midocean ridge crests. *Journal of Geophysical Research: Solid Earth*, *84*(B9), 4713-4729. https://doi.org/10.1029/JB084iB09p04713

Contreras-Reyes, E., Grevemeyer, I., Watts, A. B., Planert, L., Flueh, E. R., & Peirce, C. (2010). Crustal intrusion beneath the Louisville hotspot track. *Earth and Planetary Science Letters*, *289*(3-4), 323-333. https://doi.org/10.1016/j.epsl.2009.11.020

Davy, R. G., Collier, J. S., Henstock, T. J., & The VoiLA Consortium. (2020). Wide-angle seismic imaging of two modes of crustal accretion in mature Atlantic Ocean crust. *Journal of Geophysical Research: Solid Earth*, *125*(6), e2019JB019100. https://doi.org/10.1029/2019JB019100

Detrick, R. S., & Purdy, G. M. (1980). The crustal structure of the Kane fracture zone from seismic refraction studies. *Journal of Geophysical Research: Solid Earth*, *85*(B7), 3759-3777. https://doi.org/10.1029/JB085iB07p03759

Detrick, R. S., White, R. S., & Purdy, G. M. (1993). Crustal structure of North Atlantic fracture zones. *Reviews of Geophysics*, *31*(4), 439-458. https://doi.org/10.1029/93RG01952

Dietz, R. S., & Menard, H. W. (1953). Hawaiian swell, deep, and arch, and subsidence of the Hawaiian Islands. *The Journal of Geology*, *61*(2), 99-113. https://doi.org/10.1086/626059

Dunn, R. A., & Hernandez, O. (2009). Tracking blue whales in the eastern tropical Pacific with an ocean-bottom seismometer and hydrophone array. *The Journal of the Acoustical Society of America*, *126*(3), 1084-1094. https://doi.org/10.1121/1.3158929

Dunn, R. A., Lekić, V., Detrick, R. S., & Toomey, D. R. (2005). Three-dimensional seismic structure of the Mid-Atlantic Ridge (35°N): Evidence for focused melt supply and lower crustal dike injection, *Journal of Geophysical Research: Solid Earth*, *110*(B9). https://doi.org/10.1029/2004JB003473

Dunn, R. A., A. B. Watts, C. Xu, and D. J. Shillington (2023). A seismic tomography, gravity, and flexure study of the crust and upper mantle structure across the Hawaiian Ridge, Part 2 Ka‘ena. *Journal of Geophysical Research: Solid Earth*, MS# 2023JB028118.

Eakins, B. W., & Robinson, J. E. (2006). Submarine geology of Hana Ridge and Haleakala Volcano's northeast flank, Maui. *Journal of volcanology and geothermal research*, *151*(1-3), 229-250. https://doi.org/10.1016/j.jvolgeores.2005.07.034

Faichney, I. D., Webster, J. M., Clague, D. A., Paduan, J. B., & Fullagar, P. D. (2010). Unraveling the tilting history of the submerged reefs surrounding Oahu and the Maui-Nui Complex, Hawaii. *Geochemistry, Geophysics, Geosystems*, *11*(7). https://doi.org/10.1029/2010GC003044

Flinders, A.F., Ito, G., Garcia, M.O., Sinton, J.M., Kauahikaua, J., Taylor, B., 2013. Intrusive dike complexes, cumulate cores, and the extrusive growth of Hawaiian volcanoes. *Geophysical Research Letters*, *40*, 3367-3373. https://doi.org/10.1002/grl.50633

Fornari, D. J., & Campbell, J. F. (1987). Submarine topography around the Hawaiian Islands. *U.S. Geological Survey Professional Paper*, *1350*, 109-124

Furumoto, A. S., & Woollard, G. P. (1965). Seismic refraction studies of the crustal structure of the Hawaiian Archipelago, *Pacific Science*, *19*, 315-319.

Garcia, M. O., Hanano, D., Flinders, A., Weis, D., Ito, G., & Kurz, M. D. (2012). Age, geology, geophysics, and geochemistry of Mahukona Volcano, Hawaii. *Bulletin of Volcanology*, *74*(6), 1445-1463. https://doi.org/10.1007/s00445-012-0602-4

Garcia, M. O., Haskins, E. H., Stolper, E. M., & Baker, M. (2007). Stratigraphy of the Hawai‘i Scientific Drilling Project core (HSDP2): Anatomy of a Hawaiian shield volcano. *Geochemistry, Geophysics, Geosystems*, *8*(2). https://doi.org/10.1029/2006GC001379

Grevemeyer, I., Kaul, N., Villinger, H., & Weigel, W. (1999). Hydrothermal activity and the evolution of the seismic properties of upper oceanic crust. *Journal of Geophysical Research: Solid Earth*, *104*(B3), 5069-5079. https://doi.org/10.1029/1998JB900096

Grevemeyer, I., Ranero, C. R., & Ivandic, M. (2018). Structure of oceanic crust and serpentinization at subduction trenches. *Geosphere*, *14*(2), 395–418. https://doi.org/10.1130/GES01537.1

Growe, K., Grevemeyer, I., Singh, S. C., Marjanović, M., Gregory, E. P., Papenberg, C., et al. (2021). Seismic structure of the St. Paul Fracture Zone and Late Cretaceous to Mid Eocene oceanic crust in the equatorial Atlantic Ocean near 18° W. *Journal of Geophysical Research: Solid Earth*, *126*(11), e2021JB022456. https://doi.org/10.1029/2021JB022456

Gunn, R. (1943). A quantitative study of isobaric equilibrium and gravity anomalies in the Hawaiian Islands. *Journal of the Franklin Institute*, *236*(4), 373-390. https://doi.org/10.1016/S0016-0032(43)90275-3

Hamilton, E. L. (1957). Marine geology of the southern Hawaiian Ridge. *Geological Society of America Bulletin*, *68*(8), 1011-1026. https://doi.org/10.1130/0016-7606(1957)68[1011:MGOTSH]2.0.CO;2

Hammer, P. T. C., Dorman, L. M., Hildebrand, J. A., & Cornuelle, B. D. (1994), Jasper Seamount structure: Seafloor seismic refraction tomography, *Journal of Geophysical Research: Solid Earth*, *99*(B4), 6731-6752. https://doi.org/10.1029/93JB02170

Hanyu, T., Johnson, K. T., Hirano, N., & Ren, Z. Y. (2007). Noble gas and geochronology study of the Hana Ridge, Haleakala volcano, Hawaii; implications to the temporal change of magma source and the structural evolution of the submarine ridge. *Chemical Geology*, *238*(1-2), 1-18. https://doi.org/10.1016/j.chemgeo.2006.09.008

Hauri, E. H., Lassiter, J. C., & DePaolo, D. J. (1996). Osmium isotope systematics of drilled lavas from Mauna Loa, Hawaii. *Journal of Geophysical Research: Solid Earth*, *101*(B5), 11793-11806. https://doi.org/10.1029/95JB03346

Hein, J. R., Gibbs, A. E., Clague, D. A., & Torresan, M. (1996). Hydrothermal mineralization along submarine rift zones, Hawaii. *Marine Georesources & Geotechnology*, *14*(2), 177-203. https://doi.org/10.1080/10641199609388310

HI-Emperor (2019). Seismic imaging of volcano construction, underplating and flexure along the Hawaiian-Emperor Seamount. [Data Set] https://ds.iris.edu/mda/18-015/

Hill, D. P. (1969). Crustal structure of the island of Hawaii from seismic-refraction measurements. *Bulletin of the Seismological Society of America*, *59*(1), 101-130. https://doi.org/10.1785/BSSA0590010101

Houtz, R. E., & Ewing, J. I. (1976), Upper crustal structure as a function of plate age, *Journal of Geophysical Research*, *81*(14), 2490-2498. https://doi.org/10.1029/JB081i014p02490

Huang, S., Abouchami, W., Blichert-Toft, J., Clague, D. A., Cousens, B. L., Frey, F. A., et al. (2009). Ancient carbonate sedimentary signature in the Hawaiian plume: evidence from Mahukona volcano, Hawaii. *Geochemistry, Geophysics, Geosystems*, *10*(8). https://doi.org/10.1029/2009GC002418

James, D. E., & Savage, M. K. (1990). A search for seismic reflections from the top of the oceanic crust beneath Hawaii. *Bulletin of the Seismological Society of America*, *80*(3), 675-701. https://doi.org/10.1785/BSSA0800030675

Karson, J. A., & Dick, H. J. B. (1983). Tectonics of ridge-transform intersections at the Kane fracture zone. *Marine Geophysical Researches*, *6*(1), 51-98. https://doi.org/10.1007/BF00300398

Klein, F. W. (2016). Lithospheric flexure under the Hawaiian volcanic load: Internal stresses and a broken plate revealed by earthquakes. *Journal of Geophysical Research: Solid Earth*, *121*(4), 2400-2428. https://doi.org/10.1002/2015JB012746

Leahy, G. M., Collins, J. A., Wolfe, C. J., Laske, G., & Solomon, S. C. (2010). Underplating of the Hawaiian Swell: evidence from teleseismic receiver functions. *Geophysical Journal International*, *183*(1), 313-329. https://doi.org/10.1111/j.1365-246X.2010.04720.x

Leslie, S. C., Moore, G. F., Morgan, J. K., & Hills, D. J. (2002). Seismic stratigraphy of the Frontal Hawaiian Moat: implications for sedimentary processes at the leading edge of an oceanic hotspot trace. *Marine Geology*, *184*(1-2), 143-162. https://doi.org/10.1016/S0025-3227(01)00284-5

Lipman, P. W., & Calvert, A. T. (2011). Early growth of Kohala volcano and formation of long Hawaiian rift zones. *Geology*, *39*(7), 659-662. https://doi.org/10.1130/G31929.1

Lipman, P. W., Normark, W. R., Moore, J. G., Wilson, J. B., & Gutmacher, C. E. (1988). The giant submarine Alika debris slide, Mauna Loa, Hawaii. *Journal of Geophysical Research: Solid Earth*, *93*(B5), 4279-4299. https://doi.org/10.1029/JB093iB05p04279

Manríquez, P., Contreras-Reyes, E., & Osses, A. (2014). Lithospheric 3-D flexure modelling of the oceanic plate seaward of the trench using variable elastic thickness. *Geophysical Journal International*, *196*(2), 681-693. https://doi.org/10.1093/gji/ggt464

Lambeck, K. (1981). Flexure of the ocean lithosphere from island uplift, bathymetry and geoid height observations: the Society Islands. *Geophysical Journal International*, *67*(1), 91-114. https://doi.org/10.1111/j.1365-246X.1981.tb02734.x

Lonsdale, P. (1983). Overlapping rift zones at the 5.5 S offset of the East Pacific Rise. *Journal of Geophysical Research: Solid Earth*, *88*(B11), 9393-9406. https://doi.org/10.1029/JB088iB11p09393

Marjanović, M., Singh, S. C., Gregory, E. P., Grevemeyer, I., Growe, K., Wang, Z., et al. (2020). Seismic crustal structure and morphotectonic features associated with the Chain Fracture Zone and their role in the evolution of the equatorial Atlantic region. *Journal of Geophysical Research: Solid Earth*, *125*(10), e2020JB020275. https://doi.org/10.1029/2020JB020275

Matthews, K. J., Müller, R. D., Wessel, P., & Whittaker, J. M. (2011). The tectonic fabric of the ocean basins. *Journal of Geophysical Research: Solid Earth*, *116*(B12). https://doi.org/10.1029/2011JB008413

McMurtry, G. M., Herrero-Bervera, E., Cremer, M. D., Smith, J. R., Resig, J., Sherman, C., et al. (1999). Stratigraphic constraints on the timing and emplacement of the Alika 2 giant Hawaiian submarine landslide. *Journal of Volcanology and Geothermal Research*, *94*(1-4), 35-58. https://doi.org/10.1016/S0377-0273(99)00097-9

McNutt, M., Fischer, K., Kruse, S., & Natland, J. (1989). The origin of the Marquesas fracture zone ridge and its implications for the nature of hot spots. *Earth and Planetary Science Letters*, *91*(3-4), 381-393. https://doi.org/10.1016/0012-821X(89)90012-5

Minshull, T. A., & Charvis, P. H. (2001). Ocean island densities and models of lithospheric flexure. *Geophysical Journal International*, *145*(3), 731-739. https://doi.org/10.1046/j.0956-540x.2001.01422.x

Minshull, T. A., White, R. S., Mutter, J. C., Buhl, P., Detrick, R. S., Williams, C. A., et al. (1991). Crustal structure at the Blake Spur fracture zone from expanding spread profiles. *Journal of Geophysical Research: Solid Earth*, *96*(B6), 9955-9984. https://doi.org/10.1029/91JB00431

Moore, J. G. (1970). Relationship between subsidence and volcanic load, Hawaii. *Bulletin Volcanologique*, *34*, 562-576. https://doi.org/10.1007/BF02596771

Moore, J. G., & Clague, D. A. (2004). Hawaiian submarine manganese-iron oxide crusts—A dating tool? *Geological Society of America Bulletin*, *116*(3-4), 337-347. https://doi.org/10.1130/B25304.1

Moore, J. G., & Clague, D. A. (1992). Volcano growth and evolution of the island of Hawaii. *Geological Society of America Bulletin*, *104*(11), 1471-1484. https://doi.org/10.1130/0016-7606(1992)104<1471:VGAEOT>2.3.CO;2

Moore, J. G., Clague, D. A., Ludwig, K. R., & Mark, R. K. (1990). Subsidence and volcanism of the Haleakala Ridge, Hawaii. *Journal of Volcanology and Geothermal Research*, *42*(3), 273-284. https://doi.org/10.1016/0377-0273(90)90004-Y

Moore, J. G., Ingram, B. L., Ludwig, K. R., & Clague, D. A. (1996). Coral ages and island subsidence, Hilo drill hole. *Journal of Geophysical Research: Solid Earth*, *101*(B5), 11599-11605. https://doi.org/10.1029/95JB03215

Morgan, W. J. (1971). Convection plumes in the lower mantle. *Nature*, *230*(5288), 42-43. https://doi.org/10.1038/230042a0

OBSIC (2022). Ocean Bottom Seismic Instrument Center. https://obsic.whoi.edu.

Olson, P., Reynolds, E., Hinnov, L., & Goswami, A. (2016). Variation of ocean sediment thickness with crustal age. *Geochemistry, Geophysics, Geosystems*, *17*, 1349–1369. https://doi.org/10.1002/2015GC006143

Park, J., Morgan, J. K., Zelt, C. A., & Okubo, P. G. (2009). Volcano-tectonic implications of 3-D velocity structures derived from joint active and passive source tomography of the island of Hawaii. *Journal of Geophysical Research: Solid Earth*, *114*(B9). https://doi.org/10.1029/2008JB005929

Park, J., Morgan, J. K., Zelt, C. A., Okubo, P. G., Peters, L., & Benesh, N. (2007). Comparative velocity structure of active Hawaiian volcanoes from 3-D onshore–offshore seismic tomography. *Earth and Planetary Science Letters*, *259*(3-4), 500-516. https://doi.org/10.1016/j.epsl.2007.05.008

Park, J., & Rye, D. M. (2019). Why is crustal underplating beneath many hot spot islands anisotropic? *Geochemistry, Geophysics, Geosystems*, *20*(11), 4779-4809. https://doi.org/10.1029/2019GC008492

Raitt, R.W. (1963). The crustal rocks, in The Sea, Vol. 3, ed. M.N. Hill, Interscience, New York, 85-102.

Pockalny, R. A., Gente, P., & Buck, R. (1996). Oceanic transverse ridges: A flexural response to fracture-zone–normal extension. *Geology*, *24*(1), 71-74. https://doi.org/10.1130/0091-7613(1996)024<0071:OTRAFR>2.3.CO;2

R^{2}R (2023). Rolling Deck to Repository. [Data Set] https://www.rvdata.us/search/cruise/MGL1806.

Rees, B. A., Detrick, R., & Coakley, B. J. (1993). Seismic stratigraphy of the Hawaiian flexural moat. *Geological Society of America Bulletin*, *105*(2), 189-205. https://doi.org/10.1130/0016-7606(1993)105<0189:SSOTHF>2.3.CO;2

Ren, Z. Y., Shibata, T., Yoshikawa, M., Johnson, K. T., & Takahashi, E. (2006). Isotope compositions of submarine Hana Ridge lavas, Haleakala volcano, Hawaii: Implications for source compositions, melting process and the structure of the Hawaiian plume. *Journal of Petrology*, *47*(2), 255-275. https://doi.org/10.1093/petrology/egi074

Ren, Z. Y., Takahashi, E., Orihashi, Y., & Johnson, K. T. (2004). Petrogenesis of tholeiitic lavas from the submarine Hana Ridge, Haleakala Volcano, Hawaii. *Journal of Petrology*, *45*(10), 2067-2099. https://doi.org/10.1093/petrology/egh076

Rowley, J. S. (2017). Voyage Report: Rapid Assessment of the Geologist and Lōʻihi Seamounts. https://doi.org/10.13140/RG.2.2.28815.59044

Rychert, C. A., Laske, G., Harmon, N., & Shearer, P. M. (2013). Seismic imaging of melt in a displaced Hawaiian plume. *Nature Geoscience*, *6*(8), 657-660. https://doi.org/10.1038/ngeo1878

SAGE (2023). Seismological Facility for the Advancement of Geoscience. https://www.iris.edu/hq/

Sandwell, D., & Schubert, G. (1982). Lithospheric flexure at fracture zones. *Journal of Geophysical Research: Solid Earth*, *87*(B6), 4657-4667. https://doi.org/10.1029/JB087iB06p04657

Searle, R. C., Holcomb, R. T., Wilson, J. B., Holmes, M. L., Whittington, R. J., Kappel, E. S., et al. (1993). The Molokai fracture zone near Hawaii, and the Late Cretaceous change in Pacific/Farallon spreading direction. *Washington DC American Geophysical Union Geophysical Monograph Series*, *77*, 155-169. https://doi.org/ 10.1029/GM077p0155

Seton, M., Müller, R. D., Zahirovic, S., Williams, S., Wright, N. M., Cannon, J., et al. (2020), A Global Data Set of Present-Day Oceanic Crustal Age and Seafloor Spreading Parameters, *Geochemistry, Geophysics, Geosystems*, *21*(10), e2020GC009214. https://doi.org/10.1029/2020GC009214

Sherrod, D. R., Sinton, J. M., Watkins, S. E., & Brunt, K. M. (2007). Geologic map of the State of Hawaiʻi. *US geological survey open-file report*, *1089*, 83.

Shor, G. G., & Pollard, D. D. (1964). Mohole site selection studies north of Maui. *Journal of Geophysical Research*, *69*(8), 1627-1637. https://doi.org/10.1029/JZ069i008p01627

Smith, J. R., Satake, K., Morgan, J. K., & Lipman, P. W. (2002). Submarine landslides and volcanic features on Kohala and Mauna Kea volcanoes and the Hana Ridge, Hawaii. *Hawaiian Volcanoes: Deep Underwater Perspectives*, *128*, 11-28.

Staudigel, H., & Schmincke, H.-U. (1984), The Pliocene seamount series of La Palma/Canary Islands, *Journal of Geophysical Research: Solid Earth*, *89*(B13), 11195-11215. https://doi.org/10.1029/JB089iB13p11195

Stolper, E. M., DePaolo, D. J., & Thomas, D. M. (1996). Introduction to special section: Hawaii scientific drilling project. *Journal of Geophysical Research: Solid Earth*, *101*(B5), 11593-11598. https://doi.org/10.1029/96JB00332

Stroup, J. B., & Fox, P. J. (1981). Geologic investigations in the Cayman Trough: evidence for thin oceanic crust along the Mid-Cayman Rise. *The Journal of Geology*, *89*(4), 395-420. https://doi.org/10.1086/628605

Suyenaga, W. (1979). Isostasy and flexure of the lithosphere under the Hawaiian Islands. *Journal of Geophysical Research: Solid Earth*, *84*(B10), 5599-5604. https://doi.org/10.1029/JB084iB10p05599

Taylor, B. (2019). Shoreline slope breaks revise understanding of Hawaiian shield volcanoes evolution. *Geochemistry, Geophysics, Geosystems*, *20*(8), 4025-4045. https://doi.org/10.1029/2019GC008436

ten Brink, U. S., & Brocher, T. M. (1987), Multichannel seismic evidence for a subcrustal intrusive complex under Oahu and a model for Hawaiian volcanism, *Journal of Geophysical Research: Solid Earth*, *92*(B13), 13687-13707. https://doi.org/10.1029/JB092iB13p13687

The MathWorks Inc. (2021). MATLAB Version: 9.11.0.1873467 (R2021b) [Software] Natick, Massachusetts: The MathWorks Inc. https://www.mathworks.com

Walcott, R. I. (1970). Flexure of the lithosphere at Hawaii. *Tectonophysics*, *9*(5), 435-446. https://doi.org/10.1016/0040-1951(70)90056-9

Walker, G. P. (1999). Volcanic rift zones and their intrusion swarms. *Journal of Volcanology and Geothermal Research*, *94*(1-4), 21-34. https://doi.org/10.1016/S0377-0273(99)00096-7

Watts, A. B., & Cochran, J. R. (1974). Gravity anomalies and flexure of the lithosphere along the Hawaiian-Emperor seamount chain. *Geophysical Journal International*, *38*(1), 119-141. https://doi.org/10.1111/j.1365-246X.1974.tb04112.x

Watts, A. B. (1976). Gravity and bathymetry in the central Pacific Ocean. *Journal of Geophysical Research*, *81*(8), 1533-1553. https://doi.org/10.1029/JB081i008p01533

Watts, A. B. (1978). An analysis of isostasy in the world's oceans 1. Hawaiian-Emperor seamount chain. *Journal of Geophysical Research: Solid Earth*, *83*(B12), 5989-6004. https://doi.org/10.1029/JB083iB12p05989

Watts, A. B. (2023). *Isostasy and Flexure of the Lithosphere*. 2nd Edition, Cambridge University Press, 520 pp.

Watts, A. B. (2018). The use of object-oriented and process-oriented methods for gravity anomaly modelling of sedimentary basins. *Geophysical Journal International*, *215*(2), 1474-1482. https://doi.org/10.1093/gji/ggy353

Watts, A. B., Grevemeyer, I., Shillington, D. J., Dunn, R. A., Boston, B., & Gómez de la Peña, L. (2021). Seismic structure, gravity anomalies and flexure along the Emperor Seamount Chain. *Journal of Geophysical Research: Solid Earth*, *126*, e2020JB021109. https://doi.org/10.1029/2020JB021109

Watts, A. B., & ten Brink, U. S. (1989). Crustal structure, flexure, and subsidence history of the Hawaiian Islands. *Journal of Geophysical Research: Solid Earth*, *94*(B8), 10473-10500. https://doi.org/10.1029/JB094iB08p10473

Watts, A. B., ten Brink, U. S., Buhl, P., & Brocher, T. M. (1985). A multichannel seismic study of lithospheric flexure across the Hawaiian–Emperor seamount chain. *Nature*, *315*(6015), 105-111. https://doi.org/10.1038/315105a0

Watts, A. B., & Talwani, M. (1975). Gravity effect of downgoing lithospheric slabs beneath island arcs. *Geological Society of America Bulletin*, *86*(1), 1-4. https://doi.org/10.1029/JB081i008p01533

Watts, A. B., Tozer, B., Harper, H., Boston, B., Shillington, D. J., & Dunn, R. (2020). Evaluation of shipboard and satellite-derived bathymetry and gravity data over seamounts in the northwest Pacific Ocean. *Journal of Geophysical Research: Solid Earth*, *125*(10), e2020JB020396. https://doi.org/10.1029/2020JB020396

Watts, A. B., & Zhong, S. (2000). Observations of flexure and the rheology of oceanic lithosphere. *Geophysical Journal International*, *142*(3), 855-875. https://doi.org/10.1046/j.1365-246x.2000.00189.x

Weigel, W., & Grevemeyer, I. (1999), The Great Meteor seamount: seismic structure of a submerged intraplate volcano, *Journal of Geodynamics*, *28*(1), 27-40. https://doi.org/10.1016/S0264-3707(98)00030-1

Wessel, P. (1993a). A reexamination of the flexural deformation beneath the Hawaiian Islands. *Journal of Geophysical Research: Solid Earth*, *98*(B7), 12177-12190. https://doi.org/10.1029/93JB00523

Wessel, P. (1993b). Observational constraints on models of the Hawaiian hot spot swell. *Journal of Geophysical Research: Solid Earth*, *98*(B9), 16095-16104. https://doi.org/10.1029/93JB01230

Wessel, P., Luis, J. F., Uieda, L., Scharroo, R., Wobbe, F., Smith, W. H. F., et al. (2019), The Generic Mapping Tools Version 6 [Software], *Geochemistry, Geophysics, Geosystems*, *20*(11), 5556-5564. https://doi.org/10.1029/2019GC008515.

White, R. S., Detrick, R. S., Sinha, M. C., & Cormier, M. H. (1984). Anomalous seismic crustal structure of oceanic fracture zones. *Geophysical Journal International*, *79*(3), 779-798. https://doi.org/10.1111/j.1365-246X.1984.tb02868.x

Wolfe, C. J., McNutt, M. K., & Detrick, R. S. (1994). The Marquesas archipelagic apron: Seismic stratigraphy and implications for volcano growth, mass wasting, and crustal underplating. *Journal of Geophysical Research: Solid Earth*, *99*(B7), 13591-13608. https://doi.org/10.1029/94JB00686

Tribble, J. S., Wilkens, R., Arvidson, R. S., Busing, C. J., & Wilkens, R. H. (1993). Sediments of the Hawaiian Arch: X-ray mineralogy and microfabric. In Wilkens, RH, Firth, J., Bender, J., et al., Proc. ODP, Sci. Results (Vol. 136, pp. 65-76).

Wilson, J. T. (1963). A possible origin of the Hawaiian Islands. *Canadian Journal of Physics*, *41*(6), 863-870. https://doi.org/10.1139/p63-094

Xu, C., Dunn, R. A., Watts, A. B., Shillington, D. J., Grevemeyer, I., Gomez de la Pena, L., et al. (2022). A seismic tomography, gravity, and flexure study of the crust and upper mantle structure of the Emperor Seamounts at Jimmu guyot. *Journal of Geophysical Research: Solid Earth*, *127*(6), e2021JB023241. https://doi.org/10.1029/2021JB023241

Zhong, S., & Watts, A. B. (2013). Lithospheric deformation induced by loading of the Hawaiian Islands and its implications for mantle rheology. *Journal of Geophysical Research: Solid Earth*, *118*, 6025–6048. https://doi.org/10.1002/2013JB010408

Zucca, J. J., Hill, D. P., & Kovach, R. L. (1982). Crustal structure of Mauna Loa volcano, Hawaii, from seismic refraction and gravity data. *Bulletin of the Seismological Society of America*, *72*(5), 1535-1550. https://doi.org/10.1785/BSSA0720051535

Figure Captions and Tables

Figure 1. (inset) Map of the north Pacific ocean showing the location of the geophysical experiment and fracture zone traces that cross the region (Matthew et al., 2011). (a) Topography map of the Hawaiian Ridge. Seismic Line 01 (solid orange line) is the focus of this study. Heavy black lines indicate locations of other seismic lines that occurred as part of this experiment, but will be presented in other work. Thin black lines indicate the location of the seismic study described in Watts et al.

(1985) (red dots indicate ESP mid-points); Green lines are the seismic lines of Shor & Pollard (1964), Furumoto & Woollard (1965), and Zucca et al. (1982). Labelled white lines represent estimated isochrons of lithospheric age (Ma) from Seton et al. (2020) (note that plate age offsets near the fracture zone are not correctly represented by the age model). (b) A free-air gravity anomaly map of the Hawaiian Ridge, overlain by the seismic experiment, as in (a). The gravity map more clearly shows the Hawaiian Moat and some portions of the Moloka‘i Fracture Zone (MFZ) system that are otherwise obscured by sediments in the bathymetric map. The black dashed lines indicate the individual lineaments of the fracture zone system.

Figure 2. Topography map of the study area showing key geologic features crossed by the seismic line. White circles represent OBS locations, spaced about 15 km apart. The seismic line, which is referred to as Line 01, was shot twice, once with airgun pulses spaced ~390 m and once with pulses spaced ~62.5 m.

Figure 3. (a) A common-receiver-gather record for station 104 and the OBS shot line, showing typical seismic phases for oceanic crust. To the north, where shots cross the Cook and Jaggar Seamounts, the travel times of the deeper seismic phases are delayed by the additional crustal material present there. (b) A common receiver gather for station 107, MCS shot line, showing both the *P2P* and *PvP* phases beneath the Jaggar Seamount. (c) A common receiver gather for station 111 (located in the moat) and the MCS shot line, showing the *P1* and *P2P* phases that are typical across the moat areas and elsewhere.

Figure 4. Common-receiver-gather records for stations located along the northern portion of the line, near strands of the MFZ. (a) Station 127 located within the moat area recorded typical seismic phases for this seismic line (see legend), but the *P3-Pn* cross-over distance is less than observed along the southern part of the line, indicating thinner crust. (b) Station 131, located just north of a prominent ridge associated with the fracture zone, shows that velocities associated with the lower oceanic crust (*P3*) are missing. The *P2-Pn* cross-over distance is ~14.5 km. A detailed version of this record (showing the individual seismograms) is shown in (c) with a different reduction velocity. Note the loss of lower crustal velocities, as well as the complicated nature of the *PmP* energy. Seafloor and basement topography effect many of the records in this area, causing local focusing and defocusing of energy, complicating the analysis.

Figure 5. Common-receiver-gather seismic records for OBSs located across the Hawaiian Ridge (as indicated by the red triangles in (d)). (a) Station 113, located on the southern slope of the edifice, shows the *Pv* seismic phase that is interpreted as a refraction within the volcanic edifice, and the secondary *P3* and *P3P* phases that presumably arise from a transition from lower V*p* to higher V*p* near the base of the edifice and near the top of the oceanic crustal layer 3. The record also illustrates the large delay on the north side of the receiver as compared to the south side in *P3P* and *PmP*/*Pn*

arrivals, indicating the increasing thickness of the edifice to the north of the receiver. Stations 119 looking south (b) and 116 looking north (c) show similar seismic phases as in (a). The internal refraction *P3* is observed to persist across most of the edifice.

Figure 6. Travel-time plot of seismic phases identified for each station. Station numbers, 101-135, indicate their position along the seismic line. The travel times for a given station extend upward and away from each station to the left and right. The shot-receiver ranges are divided by two for better phase alignment across all stations. Overall changes in crustal structure and thickness can be seen by following changes in phase and phase cross-over timing along the seismic line.

Figure 7. (a) Tomographic image of the Hawaiian Ridge and flanking oceanic crust and mantle. Lower black curve is the Moho position as determined by *PmP* and *Pn* phases. The upper black and red curve is the reflector determined by *P2P* (black) and *P3P* (red) phases. Circled capital letters indicate locations of profiles shown in Figure 10. (b) Geological interpretation of the tomographic image in (a). The shallow low-velocity layer is based on the 4.5 km/s iso-velocity contour. The upper-to-lower oceanic crustal boundary is based on the 6.5 km/s iso-velocity contour (Christeson et al., 2019). The lower heavy black line indicates the Moho position. The upper heavy gray and black curves are discussed in the text. The thin dashed black line located above the upper reflector indicates the possible position of the top of the oceanic crust as indicated by forward modelling of intermittent *P2* arrivals. Vertical exaggeration in both figures is a factor of ~7.3.

Figure 8. The 1-σ standard deviation of the tomographic models as determined by a Monte Carlo analysis, as a proxy for an estimate of the uncertainty of the tomographic image in Figure 7a. Red curves show the upper and lower reflector positions; red dashed curves are 1-σ standard deviations about the mean. This image is a composite of that determined in each of the three stages of imaging.

Figure 9. Comparison of the observed gravity anomaly along Line 01 to the calculated gravity effect of the seismic tomographic model. (a) Observed BGM-3 1 s count data (grey dots) after conversion to mGal and application of a 120 s Gaussian filter to remove 'noise' due to wave-induced ship motion. Red solid line shows an additional 1.0 km Gaussian filter. Calculated curves (dark blue lines) are based on Gardner + Nafe-Drake (solid line), Nafe-Drake (wide-dashed line) and Nafe-Drake + Christenson (narrow dashed line) empirical *P* wave velocity and density relationships. Orange lines show the gravity effect of an elastic plate model based on an average load density of 2587 (narrow dashed line), 2737 (solid line) and 2887 (wide dashed line) kg/m^3, an average infill density of 2701 kg/m^3, a crust density of 2800 kg/m^3, a mantle density of 3330 kg/m^3 and thickness T_e = 26.7 km. (b) Iso-velocity contours derived from the tomographic model at 0.5 km/s interval starting at the 3.5 km/s and ending at the 8.0 km/s contour. Light blue shading is a 'best fit' elastic plate model with a load density of 2737 kg/m^3. Dashed light blue lines show calculated flexure for a load density of 2587 kg/m^3 (upper curve) and 2887 kg/m^3 (lower curve). Grey shading show uncertainties in the depth of

the upper (top of oceanic crust) and lower (Moho) reflector. Dashed grey line shows the possible top of oceanic crust beneath the edifice as shown in Figure 7b. M = Māhukona, K = Kohala, KC = Kohala Canyon, HR = Hāna Ridge.

Figure 10. Distribution of volcanic loads and the calculated cumulative flexure in the Hawaiian Islands region. The masks use to separate the loads from the bathymetry/topography are shown by filled dots. Grey filled dots = Islands, red filled dots = Hawai‘i, and yellow filled dots = Cretaceous Seamount province. Solid white lines show the calculated flexure at 1 km interval (negative = subsidence) based on an average load density of 2737 kg/m^3, an average infill density of 2701 kg/m^3, a crust density of 2800 kg/m^3, a mantle density of 3330 kg/m^3 and a T_e of 26.7, 26.7 and 3.0 km for the islands, Hawai‘i, and Cretaceous Seamount province loads respectively. Dashed white lines outline the crest of the flexural bulge at 100 m interval (thick grey lines show the crest of the bulge): a region of uplift that flanks the area of subsidence.

Figure 11. Comparison of 1-D velocity profiles to normal Pacific oceanic crust (gray shaded area) from Grevemeyer et al. (2018). Labels indicate the position of each profile in Figure 7a. Light purple area marks variation in crustal thickness for normal Pacific oceanic crust from Grevemeyer et al. (2018). To reduce the effect of the variable thickness uppermost low-velocity layer, the tops of these profiles are referenced to the 4.5 km/s velocity contour. Profile locations: (A) south-side oceanic crust, (B) southern moat, (C) Kohala flank, (D) central Hana Ridge, (E) northern moat, and (F) north-side oceanic crust near FZ.

Table 1. List of pick types, their description, and quantity

Phase	Description	Apparent Velocity, km/s (median)	Number of Picks	Median Pick Uncertainty, ms	MAD* ms
P1	Refraction within shallow sediment layer	2.8-5.0 (3.9)	5768	20	22
P2	Refraction within seismic layer 2	5.0-6.5 (5.7)	3780	25	24
P2P	Reflection top of layer 2 (top of crust)	-	2427	45	65
P3	Refraction within seismic layer 3	6.5-7.2 (6.7)	10130	30	24
Pv	Refraction within the volcanic edifice	4.5-6.0 (5.1)	10076	30	24
P3P	Reflection top of layer 3 (below edifice)	-	1840	50	65
PmP	Reflection at the seismic Moho		12153	50	47
Pn	Refraction within the mantle	>7.7 (7.9)	13539	50	71

**1.48 times the Median Absolute Deviation*

Table 2. Summary of parameters used in the three-dimensional continuous elastic plate (flexure) models and the RMS difference between the observed and calculated depth to the top of oceanic crust and Moho and free-air gravity anomaly[*]

Model	**Te (Islands) (km)**	**Te (Cretaceous Seamount 'province') (km)**	**Te (Hawai'i) (km)**	**RMS Possible top oceanic crust (km)**	**RMS Moho (km)**	**RMS free-air gravity anomaly (mGal)**
1	26.7	26.7	26.7	1.1	0.7	15.3
2	26.7	3.0	26.7	1.1	0.6	15.3
3	26.7	3.0	10.0	1.4	0.9	34.1
4	26.7	3.0	20.0	1.3	0.7	17.3
5	26.7	3.0	30.0	1.1	0.6	17.0
6	26.7	3.0	40.0	1.0	0.8	24.1
7	26.7	3.0	50.0	1.0	1.0	34.4
8	30.0	3.0	20.0	1.3	0.6	17.3
9	30.0	3.0	30.0	1.1	0.7	17.0
10	30.0	3.0	40.0	1.0	0.9	24.1

[*]Calculations are based on an average load density of 2737 kg/m3, an average infill density of 2701 kg/m3, a crust density of 2800 kg/m3, and a mantle density of 3330 kg/m3.

Figure 1.

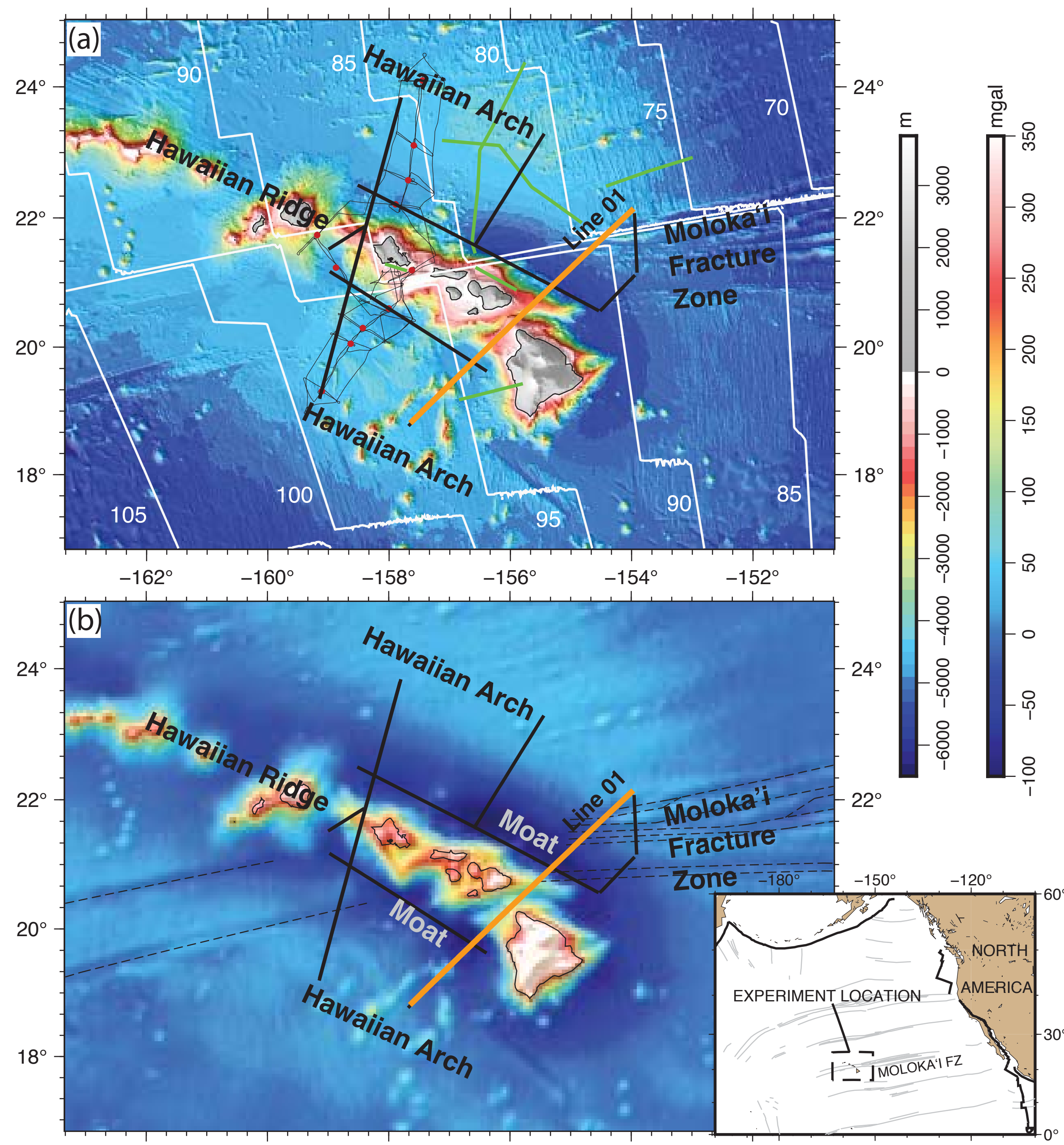
(a)
(b)
Hawaiian Arch
Hawaiian Ridge
Hawaiian Arch
Line 01
Moloka'i
Fracture
Zone
Moat
Moat
90
85
80
75
70
105
100
95
90
85
24°
22°
20°
18°
−162°
−160°
−158°
−156°
−154°
−152°
m
3000
2000
1000
0
−1000
−2000
−3000
−4000
−5000
−6000
mgal
350
300
250
200
150
100
50
0
−50
−100
−180°
−150°
−120°
60°
30°
0°
NORTH
AMERICA
EXPERIMENT LOCATION
MOLOKA'I FZ

Figure 2.

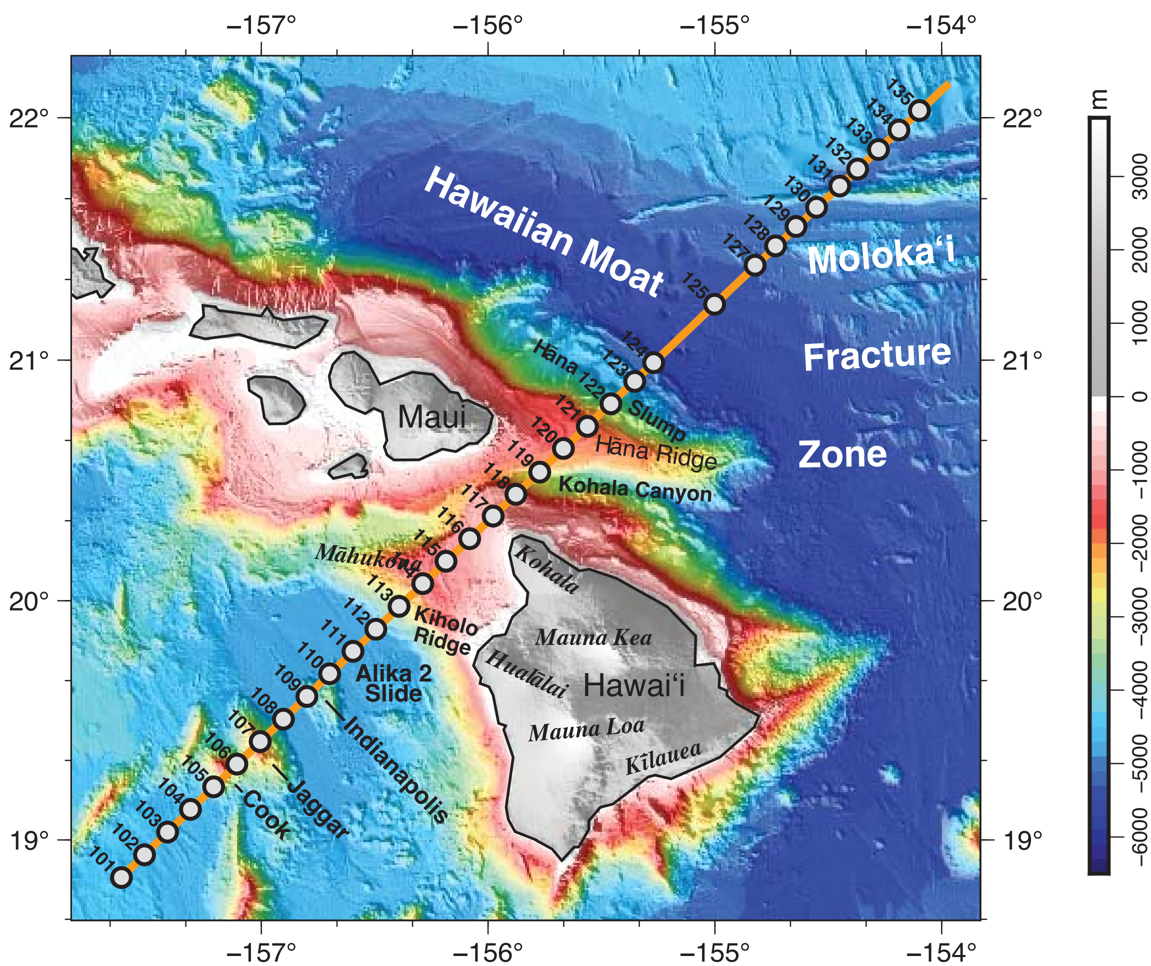

−157°
−156°
−155°
−154°
22°
21°
20°
19°
m
3000
2000
1000
0
−1000
−2000
−3000
−4000
−5000
−6000
Hawaiian Moat
Molokaʻi
Fracture
Zone
Maui
Hāna
Slump
Hāna Ridge
Kohala Canyon
Māhukona
Kohala
Kiholo
Ridge
Mauna Kea
Hualālai
Hawaiʻi
Alika 2
Slide
Mauna Loa
Kīlauea
Indianapolis
Jaggar
Cook
101
102
103
104
105
106
107
108
109
110
111
112
113
115
116
117
118
119
120
121
122
123
124
125
127
128
129
130
131
132
133
134
135

Figure 3.

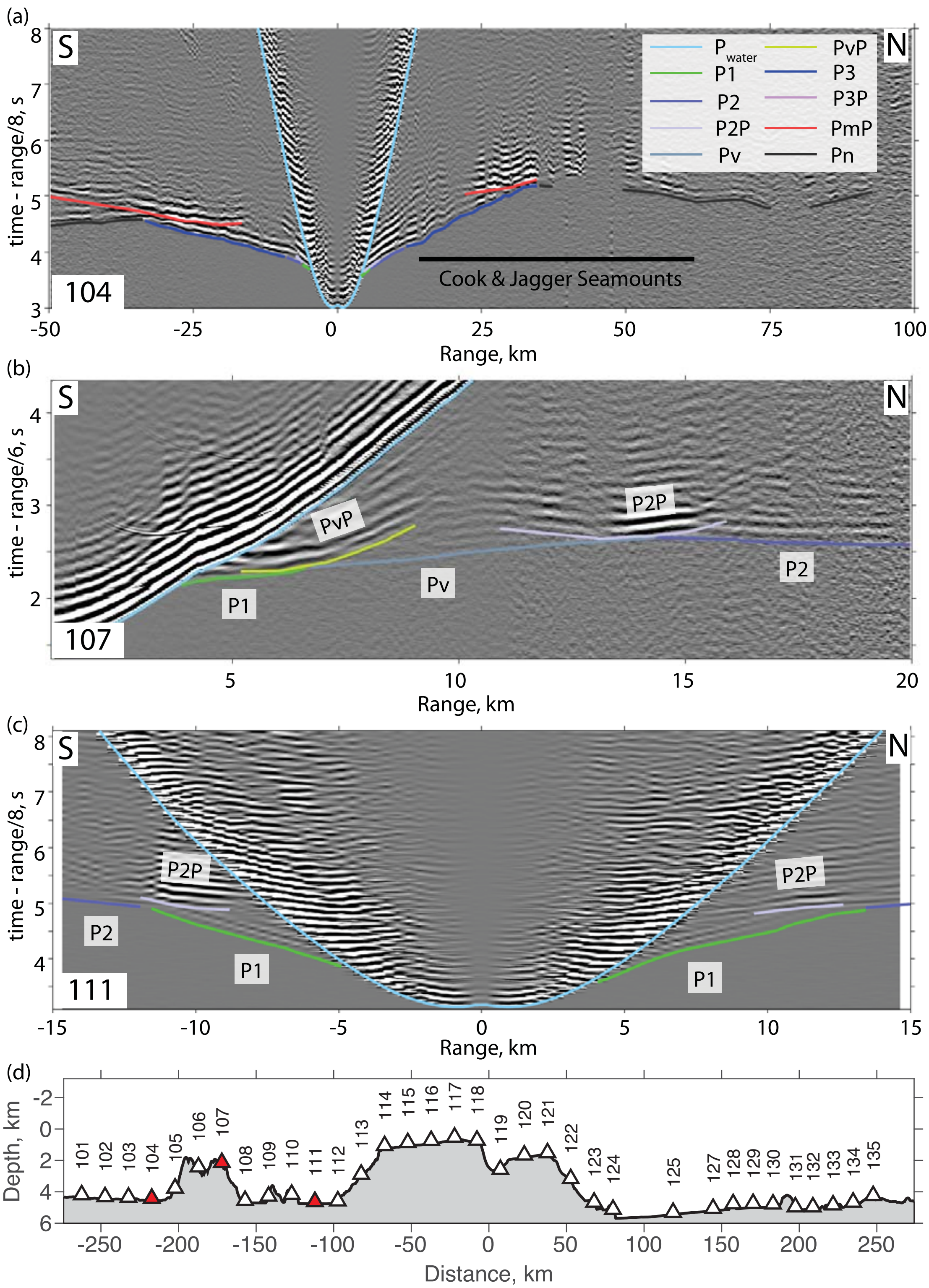
(a)
S
N
104
Cook & Jagger Seamounts
time - range/8, s
Range, km
(b)
S
N
PvP
P2P
P1
Pv
P2
107
time - range/6, s
Range, km
(c)
S
N
P2P
P2
P1
111
time - range/8, s
Range, km
(d)
Depth, km
Distance, km

Figure 4.

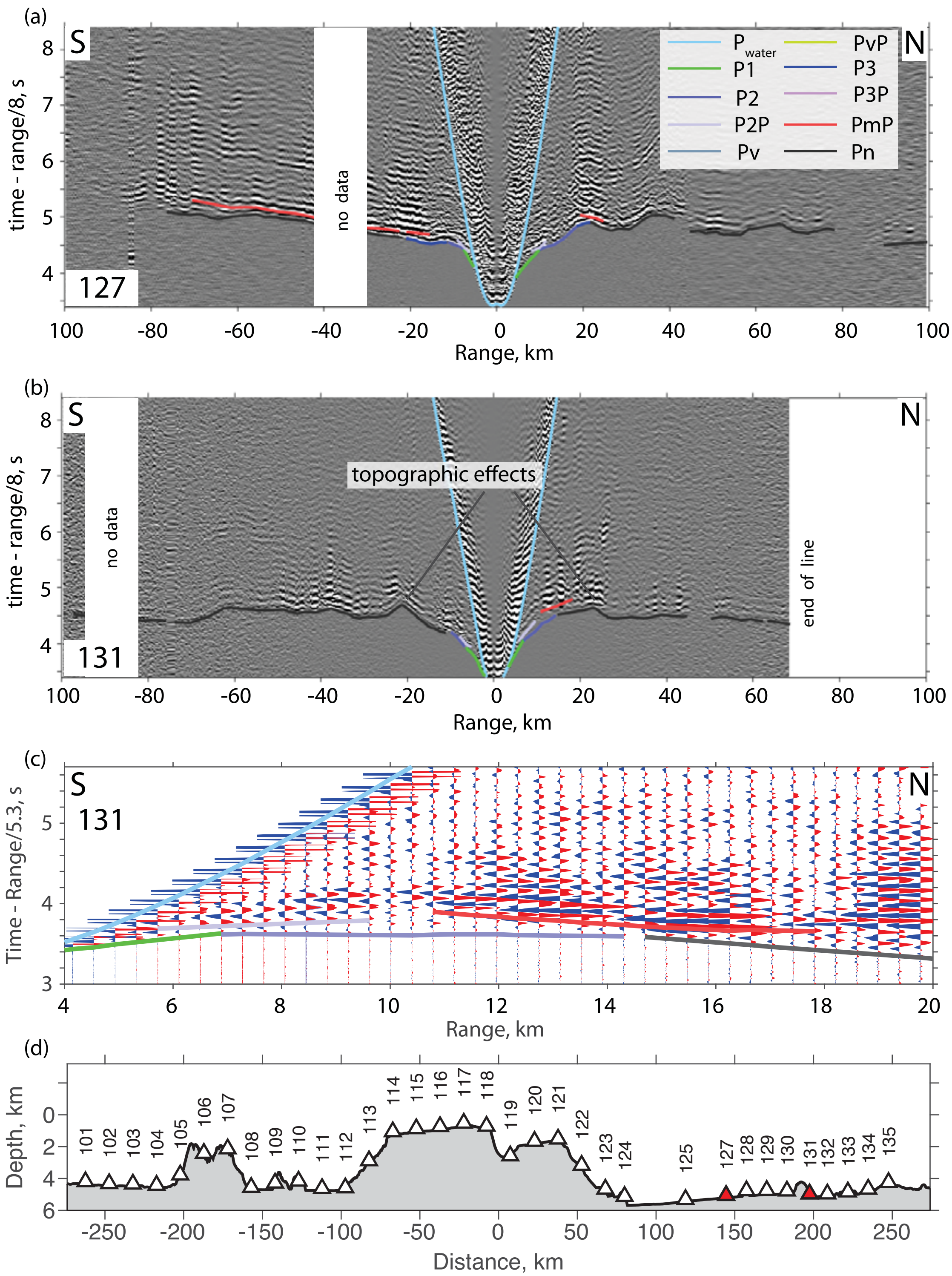

(a)
S
N
time - range/8, s
127
no data
P water
P1
P2
P2P
Pv
PvP
P3
P3P
PmP
Pn
Range, km
(b)
S
N
131
no data
topographic effects
end of line
time - range/8, s
Range, km
(c)
S
N
131
Time - Range/5.3, s
Range, km
(d)
Depth, km
Distance, km
101
102
103
104
105
106
107
108
109
110
111
112
113
114
115
116
117
118
119
120
121
122
123
124
125
127
128
129
130
131
132
133
134
135

Figure 5.

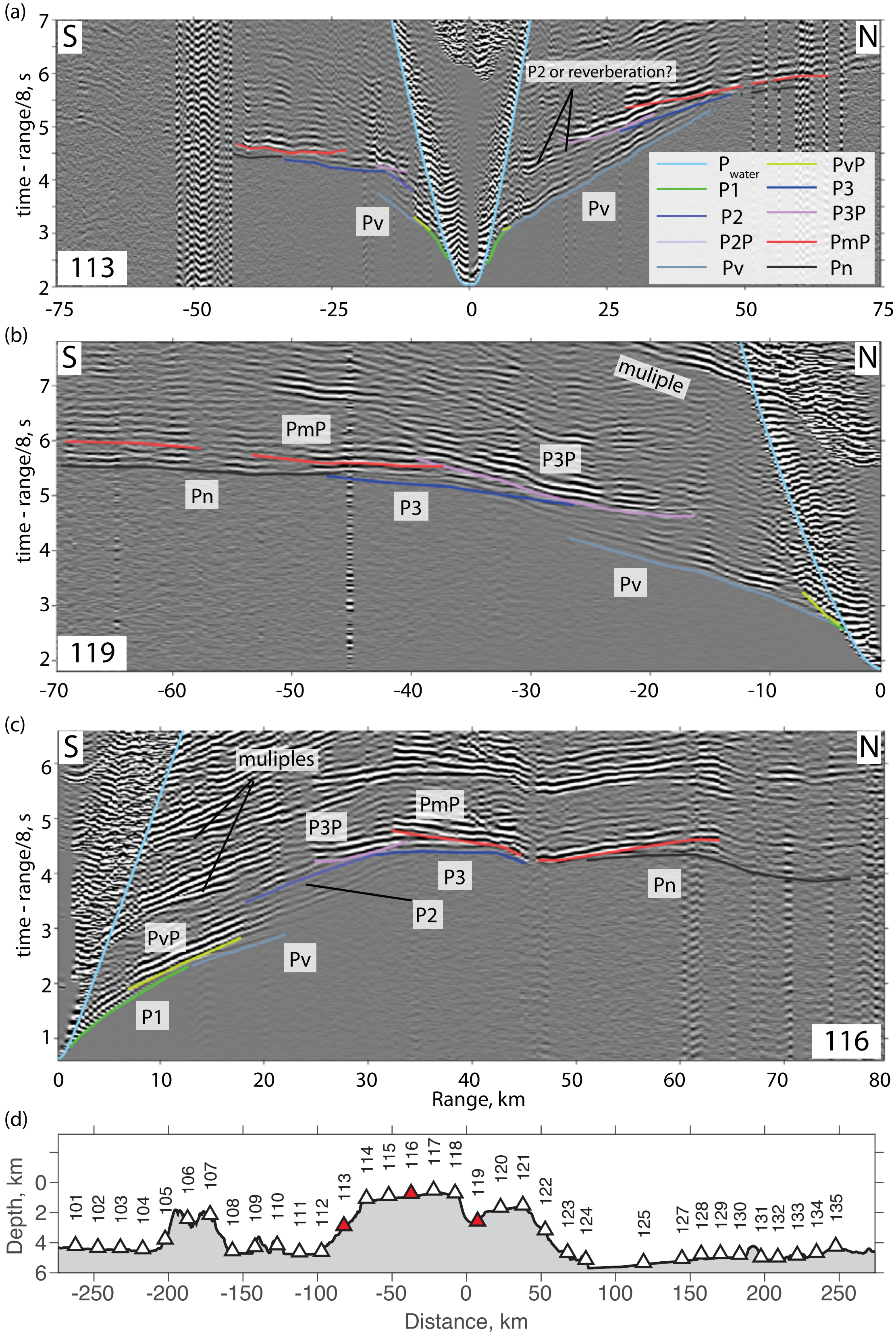

(a)
S
N
113
P2 or reverberation?
Pv
Pv
P_{water}
P1
P2
P2P
Pv
PvP
P3
P3P
PmP
Pn
time - range/8, s
(b)
S
N
119
muliple
PmP
P3P
Pn
P3
Pv
time - range/8, s
(c)
S
N
116
muliples
PmP
P3P
P3
P2
Pn
PvP
Pv
P1
time - range/8, s
Range, km
(d)
Depth, km
Distance, km
101 102 103 104 105 106 107 108 109 110 111 112 113 114 115 116 117 118 119 120 121 122 123 124 125 127 128 129 130 131 132 133 134 135

Figure 6.

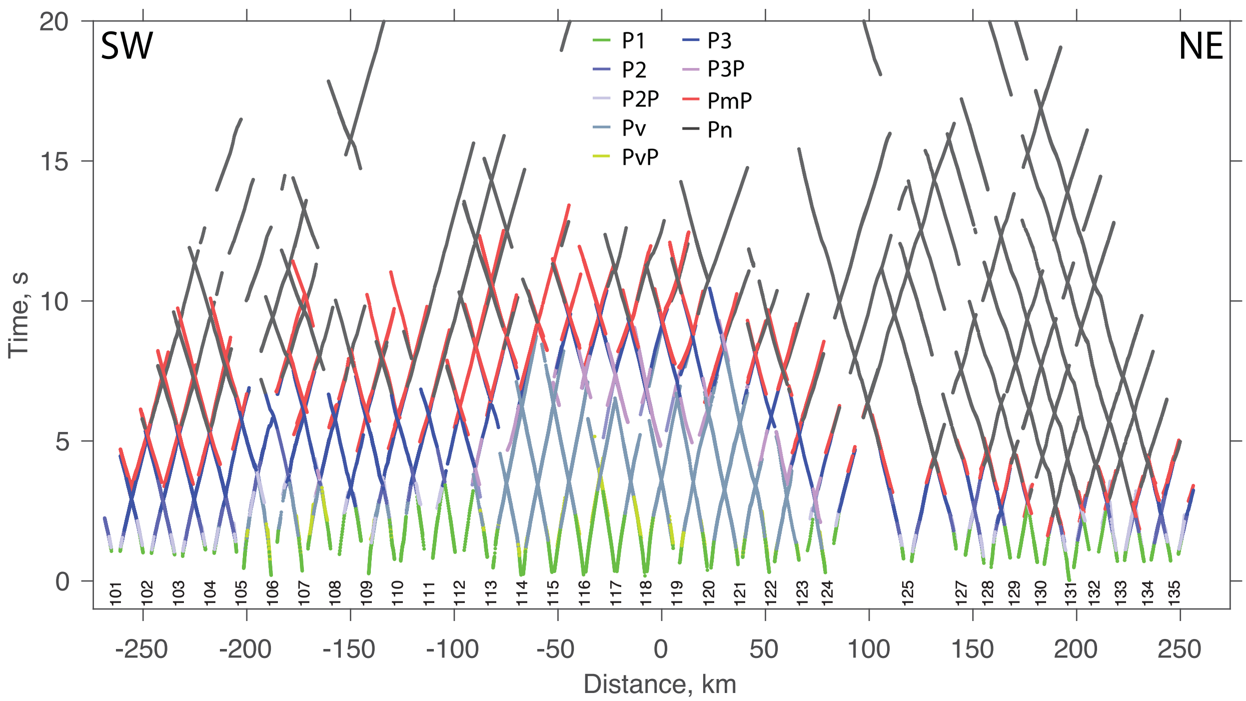

SW
NE
P1
P2
P2P
Pv
PvP
P3
P3P
PmP
Pn
Time, s
Distance, km
101
102
103
104
105
106
107
108
109
110
111
112
113
114
115
116
117
118
119
120
121
122
123
124
125
127
128
129
130
131
132
133
134
135

Figure 7.

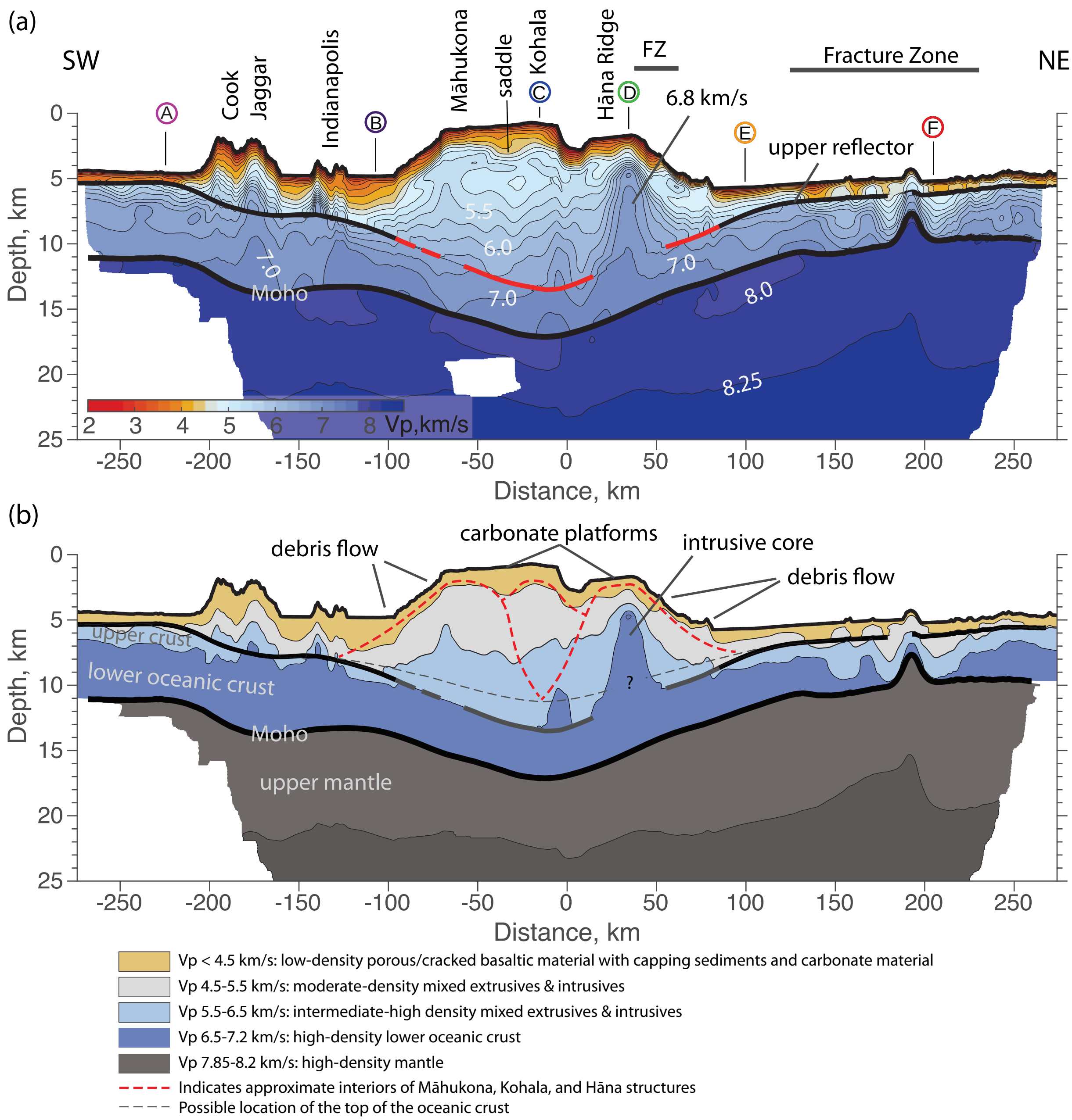

(a)
SW
NE
Cook
Jaggar
Indianapolis
Māhukona
saddle
Kohala
Hāna Ridge
FZ
Fracture Zone
A
B
C
D
E
F
6.8 km/s
upper reflector
5.5
6.0
7.0
7.0
7.0
8.0
8.25
Moho
Depth, km
Distance, km
2 3 4 5 6 7 8 Vp,km/s
(b)
debris flow
carbonate platforms
intrusive core
debris flow
upper crust
lower oceanic crust
Moho
upper mantle
?
Depth, km
Distance, km
Vp < 4.5 km/s: low-density porous/cracked basaltic material with capping sediments and carbonate material
Vp 4.5-5.5 km/s: moderate-density mixed extrusives & intrusives
Vp 5.5-6.5 km/s: intermediate-high density mixed extrusives & intrusives
Vp 6.5-7.2 km/s: high-density lower oceanic crust
Vp 7.85-8.2 km/s: high-density mantle
Indicates approximate interiors of Māhukona, Kohala, and Hāna structures
Possible location of the top of the oceanic crust

Figure 8.

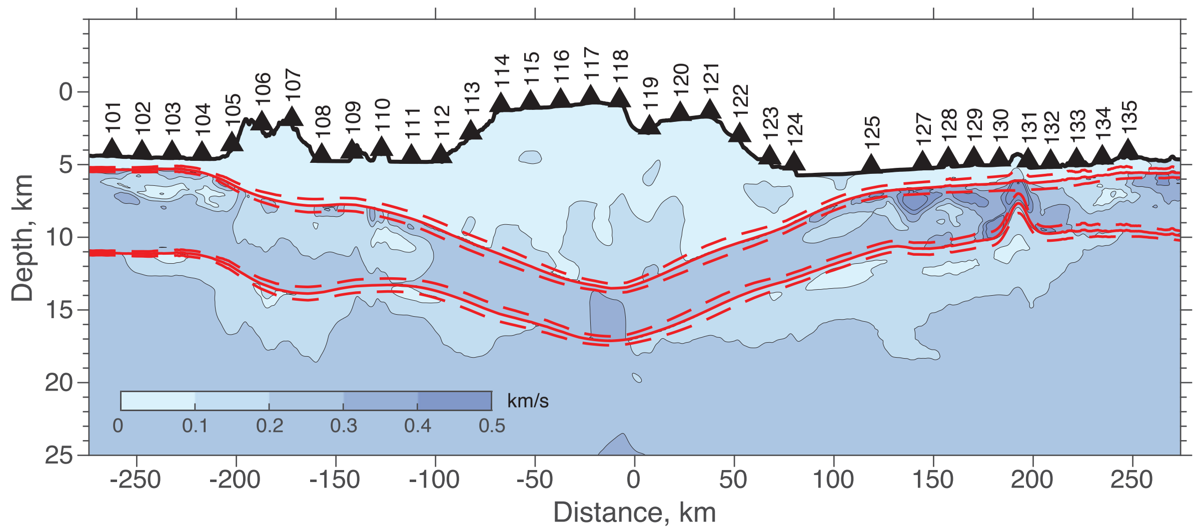

Depth, km
Distance, km
km/s
0 0.1 0.2 0.3 0.4 0.5
101 102 103 104 105 106 107 108 109 110 111 112 113 114 115 116 117 118 119 120 121 122 123 124 125 127 128 129 130 131 132 133 134 135

Figure 9.

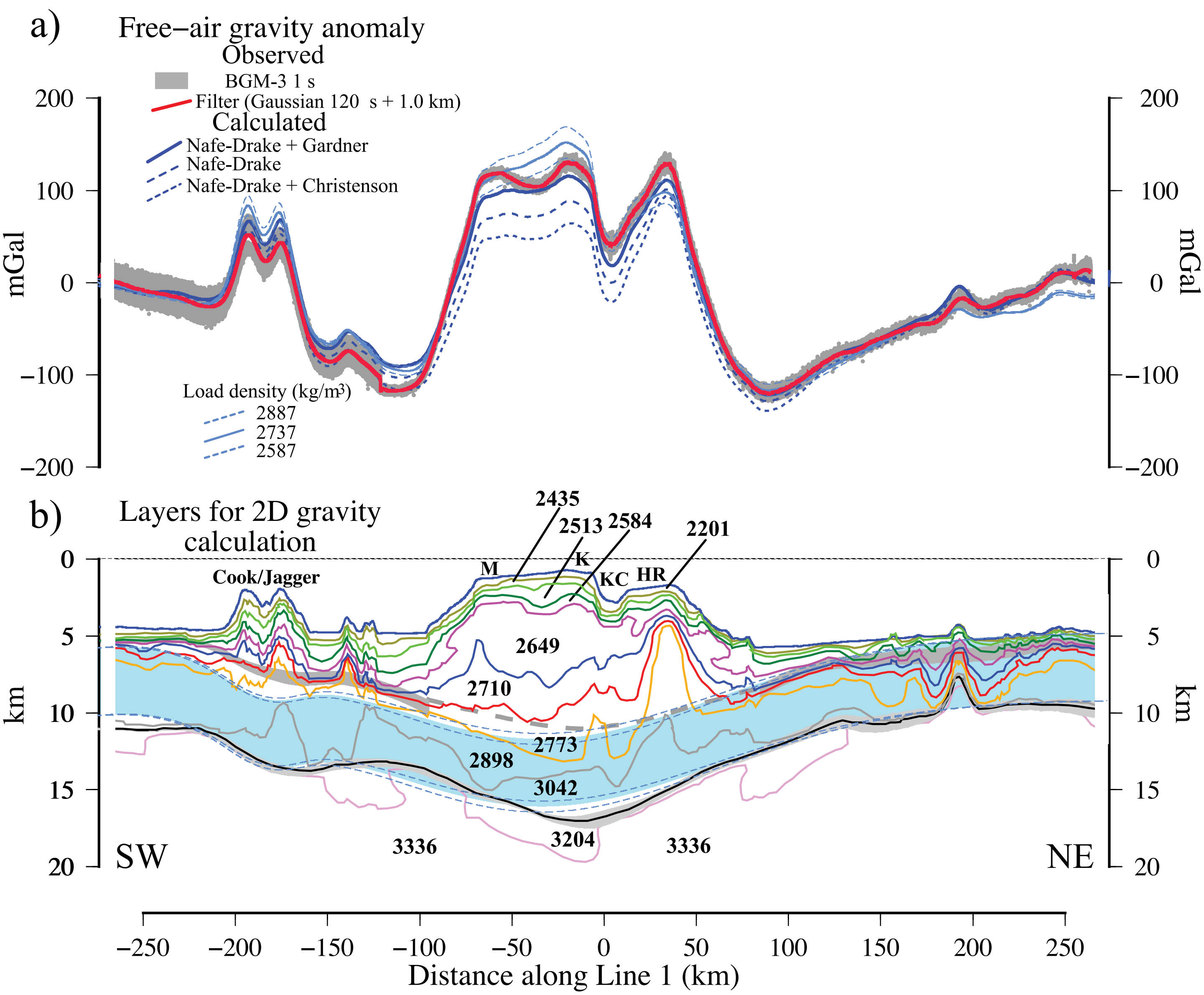
a)
Free−air gravity anomaly
Observed
BGM-3 1 s
Filter (Gaussian 120 s + 1.0 km)
Calculated
Nafe-Drake + Gardner
Nafe-Drake
Nafe-Drake + Christenson
Load density (kg/m3)
2887
2737
2587
mGal
200
100
0
−100
−200
b)
Layers for 2D gravity calculation
Cook/Jagger
M
K
KC
HR
2435
2513
2584
2201
2649
2710
2773
2898
3042
3204
3336
3336
SW
NE
km
0
5
10
15
20
−250
−200
−150
−100
−50
0
50
100
150
200
250
Distance along Line 1 (km)

Figure 10.

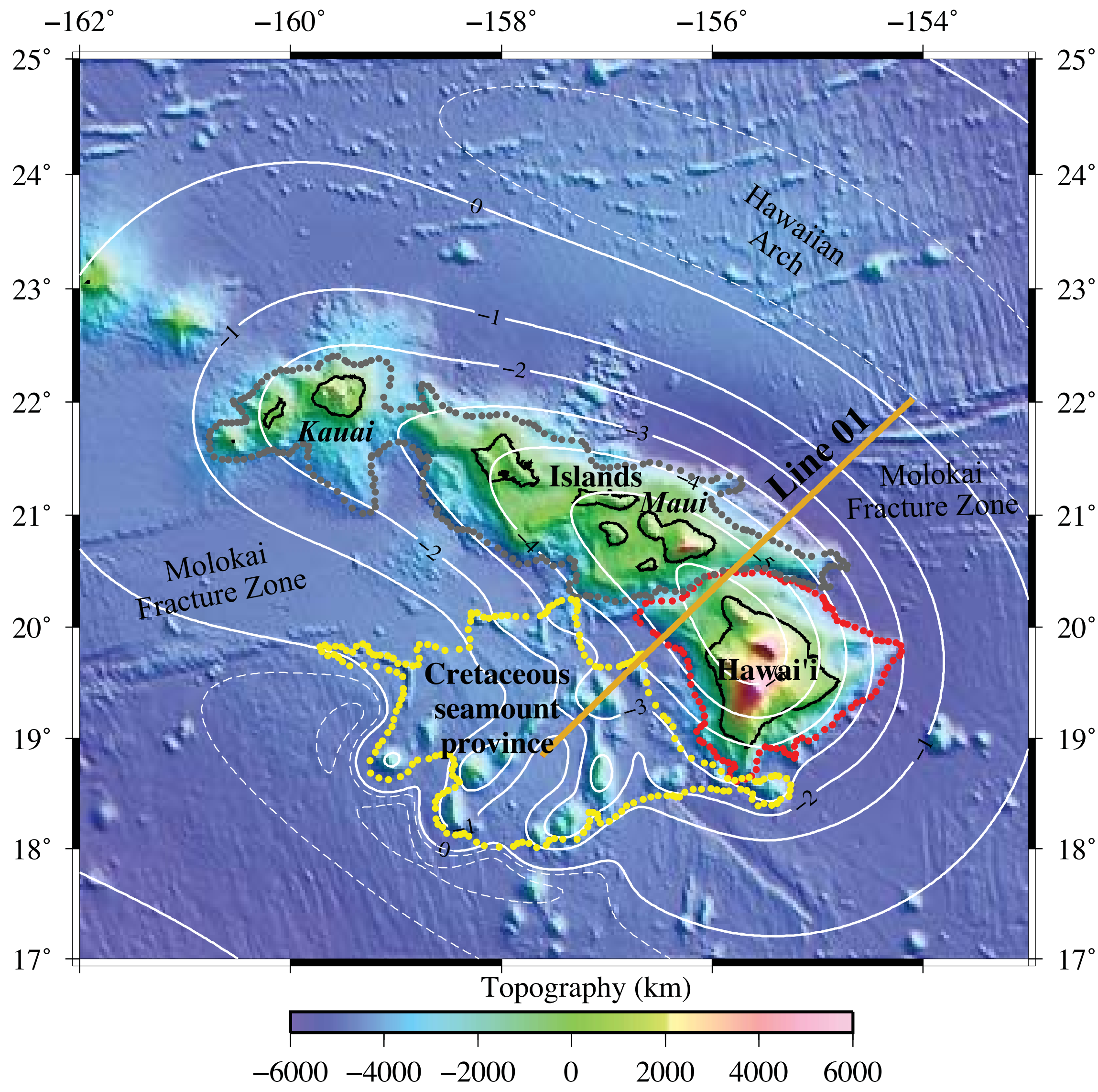

−162°
−160°
−158°
−156°
−154°
25°
24°
23°
22°
21°
20°
19°
18°
17°
Hawaiian Arch
Kauai
Islands
Maui
Line 01
Molokai Fracture Zone
Molokai Fracture Zone
Hawai'i
Cretaceous seamount province
0
−1
−2
−3
−4
−5
Topography (km)
−6000
−4000
−2000
0
2000
4000
6000

Figure 11.

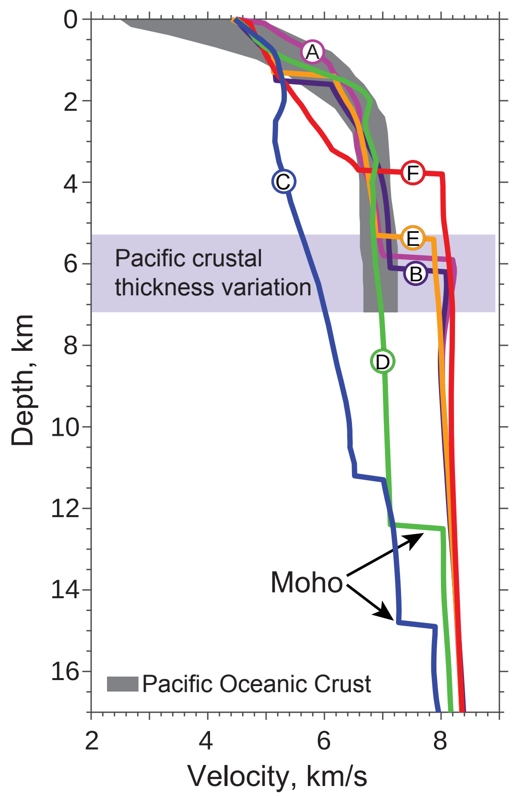

0
2
4
6
8
10
12
14
16
Depth, km
A
B
C
D
E
F
Pacific crustal
thickness variation
Moho
Pacific Oceanic Crust
2
4
6
8
Velocity, km/s